Distributed fibre optic strain sensing of an axially deformed well model in the laboratory

Tsubasa Sasaki [a], Jinho Park [b], Kenichi Soga [b], Taichi Momoki [c], Kyojiro Kawaguchi [c], Hisashi Muramatsu [c], Yutaka Imasato [c], Ajit Balagopal [d], Jerod Fontenot [d] and Travis Hall [d]

[a] Earth Sciences Division, Lawrence Berkeley National Laboratory, 1 Cyclotron Road, Berkeley, CA 94720, USA

[b] Department of Civil and Environmental Engineering, University of California–Berkeley, Berkeley, CA 94720, USA

[c] Toyo Engineering Corporation, 2 Chome-8-1 Akanehama, Narashino, Chiba 275-0024, Japan

[d] Baker Hughes, a GE company, 17021 Aldine Westfield Rd, Houston, TX 77073, USA

Abstract

Well integrity is crucial in enabling sustainable gas production from methane hydrate reservoirs and real-time distributed monitoring techniques can potentially facilitate proper and timely inspection of well integrity during gas production. In this research, the feasibility of distributed fibre optic strain monitoring with Brillouin optical time domain reflectometry/analysis (BOTDR/A) for well monitoring was examined by conducting a laboratory test on a well model subjected to axial tensile deformation, which occurs due to reservoir compaction during gas production. First, the validity of the proposed experimental methodology is assessed by a finite element analysis and theoretical modelling of a well subjected to reservoir compaction. A 3 m long well model is developed from the modelling and is instrumented with different types of fibre optic cables to measure the distributed strain development during tensile loading. Results show that the proposed well model and loading scheme can satisfactorily simulate the axial tensile deformation of the well in the laboratory condition. BOTDR is capable of capturing the tensile strain development of the well model accurately within the limitation of the spatial resolution of the BOTDR measurement. To enable accurate distributed strain monitoring of well deformation with BOTDR/A, the following issues are discussed: tightly buffered coating layers around optical fibre cores through mechanical compression and/or chemical adhesion, and a small number of coating layers.

Keywords

Wellbore integrity; Fibre optic monitoring; Methane hydrate; Reservoir compaction

1. Introduction

Methane hydrate formed in deep geologic strata has the potential to become a promising source of natural gas in the future owing to its enormous quantity (Maslin *et al.*, 2010). As such, field gas production tests have been conducted in Canada (Yamamoto and Dallimore, 2008), US (Farrell *et al.*, 2012), Japan (Yamamoto *et al.*, 2014; Yamamoto, 2015) and China (Chen *et al.*, 2018; Li *et al.*, 2018) to assess the feasibility of commercial gas production from methane hydrate reservoirs. For example, in the field gas production test at the Nankai Trough in 2013, a total of 119,500 m^3 of methane gas was produced in six days. However, the test was terminated prematurely due to sand production (Uchida, Klar and Yamamoto, 2016). One of the potential causes of sand production is considered to be well failure induced by the compaction of the unconsolidated methane hydrate reservoir (Yoneda *et al.*, 2018).

Reservoir compaction and well integrity issues are not unique to methane hydrate reservoirs but are also common in conventional oil and gas reservoirs. For example, in the Wilmington field in California, more than 300 wells were damaged (and more than 40% of them had to be abandoned) due to reservoir compaction (Roberts, 1953). Remedial operations cost nearly a hundred million dollars (Mayuga and Allen, 1969). Another example is the Ekofisk field in the North Sea, where compaction in the weak reservoir chalk layer induced buckling, tension and shear failures of the wells (Schwall and Denney, 1994). The cost of countermeasures such as lifting the subsided platforms reached approximately one billion dollars in total (Nagel, 2001). These reservoir compaction-induced well failures could have been prevented or mitigated if there had been real-time in-well deformation monitoring capabilities to detect early signs of well damage to facilitate timely countermeasures.

Distributed fibre optic monitoring technique can be effective for in-well applications due to the immunity to electromagnetic interference and high resistance to harsh environment of optical fibres. Distributed fibre optic acoustic sensing (DAS) and temperature sensing (DTS) have been deployed in the field for over a decade (Hurtig *et al.*, 1994; Molenaar *et al.*, 2012), whereas distributed fibre optic strain sensing (DSS) has been limited to pipeline monitoring. Table 1 shows a simple comparison of DAS, DTS and DSS. DTS has been used in the field for over two decades but it is exclusively for temperature monitoring. It can, however, still detect anomalies such as gas leakage through Joule-Thomson effect. DAS has been employed in the field for approximately a decade, and it is capable of monitoring acoustic signals at high measurement frequency (~ 1

kHz). However, the spatial resolution is low and it is in general incapable of measuring accurate strain or temperature change. DSS, in contrast, can measure both strain and temperature accurately with high spatial resolution. Currently, dynamic measurement with DSS is challenging but techniques to enable it are actively investigated (Peled, Motil and Tur, 2012; Zhang *et al.*, 2014; Motil, Bergman and Tur, 2016; Li *et al.*, 2017; Maraval *et al.*, 2017; Shangguan *et al.*, 2017). Therefore, DSS is the suitable distributed fibre optic measurement technique for well integrity monitoring purposes. However, DSS has not been utilised in the field as much as DAS and DTS (Baldwin, 2018; Hveding, Bukhamsin and Aramco, 2018), despite its potential to monitor well integrity effectively (Klar *et al.*, 2019).

Table 1 Basic characteristics of DAS, DTS and DSS.

	DAS	DTS	DSS
Main usage	Perforation monitoring, gas leakage detection, sand production detection.	Pipeline leak detection, in-well monitoring of liquid flow, optimization of gas lift operations.	Pipeline integrity monitoring
Advantages	Dynamic monitoring (~ 1kHz) capability	High spatial resolution (~ 1 m)	High spatial resolution (~ 0.5 m), measuring both strain and temperature
Disadvantages	Low spatial resolution (~ 10 m)	Strain cannot be monitored, slow data acquisition speed (> 5 min)	Slow data acquisition speed (> 5 min)

In order to assess the effectiveness of distributed fibre optic strain sensing technique, a feasibility study was conducted in this study in the laboratory condition prior to field implementation. One of the well deformation mechanisms during reservoir compaction, which is expected to occur in the unconsolidated methane hydrate reservoir in the Nankai Trough during gas production, is axial tensile deformation in the overburden layer. This deformation mechanism of the well is critical because the tensile deformation could cause cement failure, which in turn leads to loss of zonal isolation. Hence, the feasibility of distributed fibre optic strain monitoring for monitoring the axial tensile deformation of a well was examined in this study. Brillouin optical time domain reflectometry/analysis (BOTDR/A) is employed to carry out distributed strain measurement in the experiment. The objectives of this study are as follows:

(i) to develop a testing methodology that can simulate the axial tensile deformation of the well during reservoir compaction in the laboratory setting,

(ii) to assess the feasibility of distributed strain monitoring of the well by BOTDR/A in the

laboratory testing scheme developed in this study and,

(iii) to identify key characteristics of fibre optic cables that enable accurate strain measurements with BOTDR/A.

The laboratory test is comprised of a well model and a simple tensile loading scheme to simulate the axial tensile deformation of the model. The well model consists of an inner pipe, cement sheath and outer pipe. The cross-sectional dimensions of the model are identical to those of a typical well casing (9 5/8 in.) and borehole (12 1/4 in.) drilled in the field. The length of the model is 3.1 m (122 in.). A tensile load is applied on the outer pipe to facilitate propagation of tensile deformation from the outer pipe to cement and to the inner pipe, which are respectively representative of casing, cement sheath and formation in the field. Distributed strain monitoring is carried out by BOTDR/A with fibre optic cables installed in the annular cement of the model. The details of the laboratory testing methodology and distributed fibre optic strain monitoring method are provided in the following sections. It is noted that the outcome of this research will also be applicable to conventional oil and gas reservoirs, as the tensile well deformation is not unique to methane hydrate reservoirs but also common in conventional oil and gas reservoirs in the event to reservoir compaction.

2. Methodology

2.1. Axial failure mechanism of a wellbore

Oil and gas wells are deformed during reservoir compaction, which has caused severe well failures in the field (Roberts, 1953; Nagel, 2001). One of the well failure mechanisms is the axial failure, which is shown schematically in Figure 1 in the case of a methane hydrate reservoir. This mechanism occurs in a vertical well that is subjected to reservoir compaction; the well compresses in the reservoir layer and elongates in the overburden layer. Although the compressive deformation could lead to severe well failure such as buckling, the tensile deformation is also critical as the well cement is damaged more easily in tension than in compression (i.e., cement tensile strength is approximately one tenth of the compressive strength (Teodoriu *et al.*, 2012)). Also, the tensile failure could propagate upward along the well with the progress of reservoir compaction, inducing loss of zonal isolation. The compression failure, on the other hand, is confined within the reservoir layer. The sand production problem at the Nankai Trough (Yamamoto *et al.*, 2014, 2017; Yamamoto, 2015) could be attributed to compressive well failure in the reservoir layer rather than tensile failure in the overburden layer. However, in order to facilitate long-term gas production, tensile failure of the well (especially the cement) has to be

prevented. In addition to tensile and compressive well failures, well integrity could also be lost due to the casing-cement and/or cement-formation interface failure. Such interface failure could create a pathway for oil, gas and other formation fluids to escape toward the formation surface which might lead to serious environmental and safety problems. In the following section, tensile deformation of a well is analysed by a finite element simulation of the Nankai Trough case. In this simulation, the cement interface failure was modelled by a Coulomb friction model calibrated against laboratory test results on cement interface behaviour (Yoneda *et al.*, 2014) and it was shown that the interface failure would not occur before the tensile failure of the well. Therefore, tensile failure of the well is analysed in detail. A theoretical analysis of the tensile deformation of a well model is then carried out to identify a method to simulate the tensile well deformation mechanism in the laboratory.

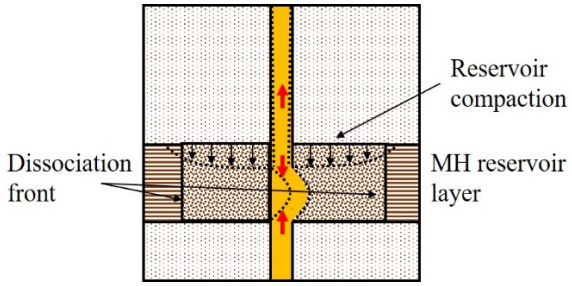

Figure 1 The axial tensile/compressive failure mechanism of the well.

2.2. Simulation of the axial tensile deformation of the well

2.2.1. Field-scale finite element analysis

A parametric study on well integrity during reservoir compaction for the Nankai Trough case is carried out by the authors and is to be presented in a separate paper (Sasaki *et al.*, 2019). Results are re-analysed herein by focusing on the mechanism of the tensile deformation of the well during reservoir compaction.

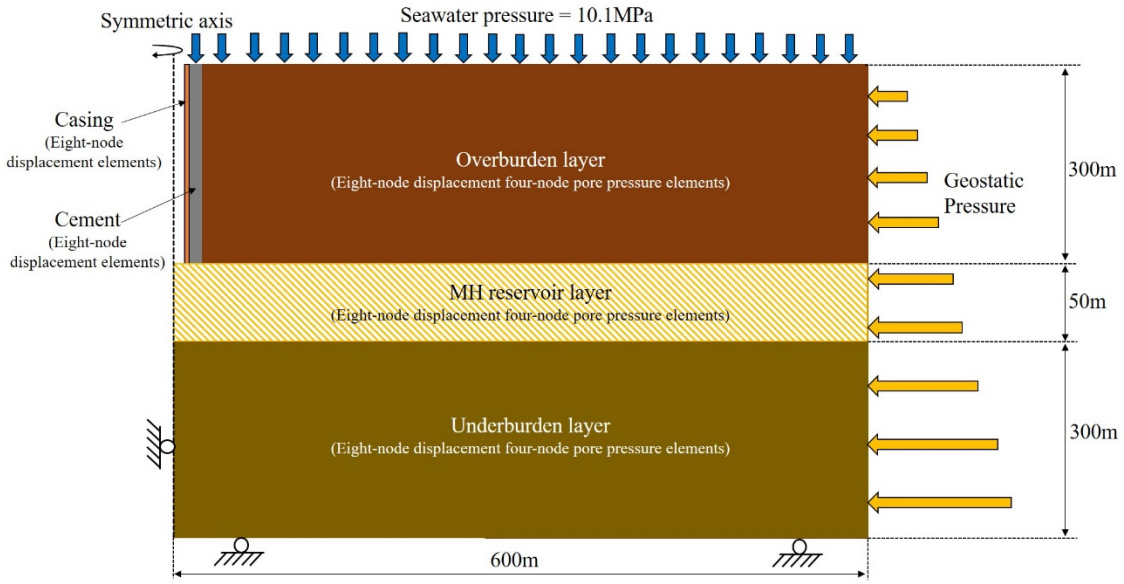

(a)

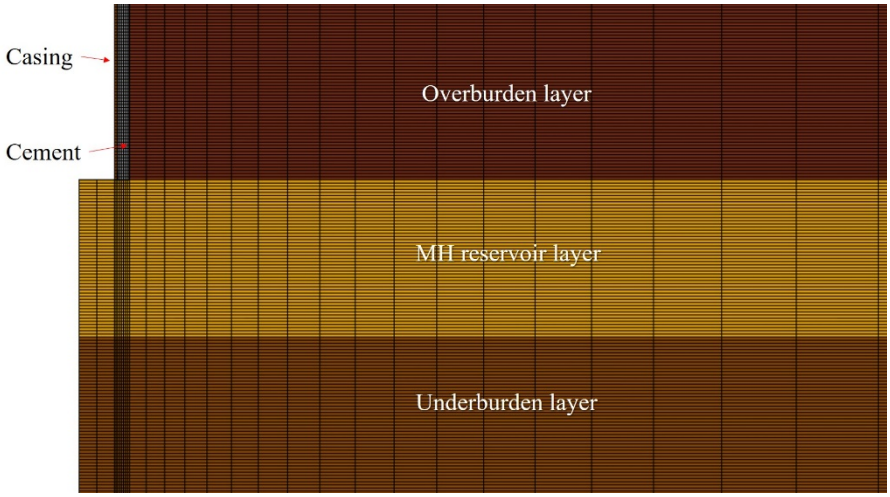

(b)

Figure 2 The axi-symmetric finite element model for simulating reservoir compaction and well integrity: (a) model geometry and boundary conditions; (b) model mesh.

Figure 2 shows the schematic of the axi-symmetric finite element model employed in the parametric study. The total depth and radial length of the model are 650 m and 600 m, respectively. The behaviour of the formation is modelled by the methane hydrate critical state (MHCS) model (Uchida, 2012; Uchida, Soga and Yamamoto, 2012), which is capable of simulating the plastic compaction of hydrate-bearing soil accurately. The validation of the performance of the MHCS model is provided in a separate paper specializing in the numerical modelling of reservoir compaction and its effect on well integrity under different reservoir compaction scenarios (Sasaki

et al., 2019). The well consists of casing and cement, which are both modelled as elasto-plastic material, and it is located in the overburden layer (0 m–300 m). The methane hydrate reservoir layer is located in the mid-depth of the model (300 m–350 m). Zero lateral and vertical displacement boundaries are specified on the left and bottom edges of the formation, respectively, while constant pressure boundaries are imposed on the top and right edges of the formation. The contact behaviour at the casing-cement and cement-formation interfaces is modelled by the penalty method in the contact normal direction and by the Coulomb friction model in the contact tangential direction, respectively. Since the interface behaviour is crucial to simulating well integrity during reservoir compaction, the validation of the behaviour of the interface model is carried out (Sasaki *et al.*, 2019), which shows that the performance of the interface model is satisfactory compared to the laboratory experiment results presented in this paper. The strength of the casing is set to a constant value (Mises model), whereas the strength of the cement increases with increasing mean stress level of the cement (Mohr-Coulomb model). As to the formation, not only the strength but also the stiffness is proportional to the mean stress level of the formation (MHCS model).

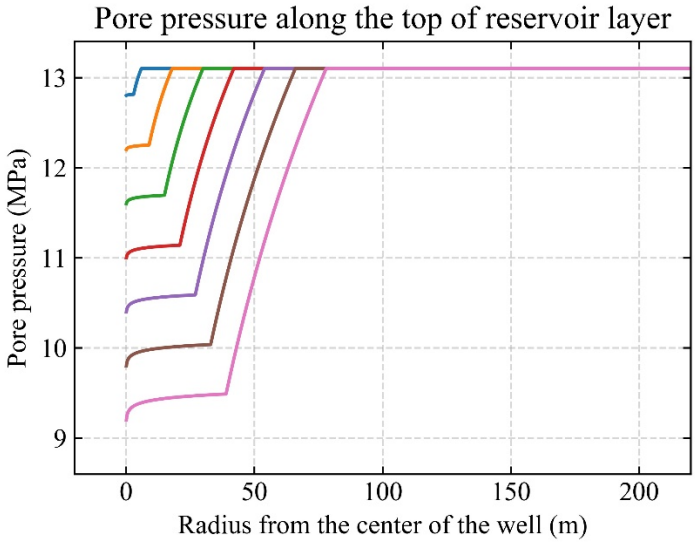

(a)

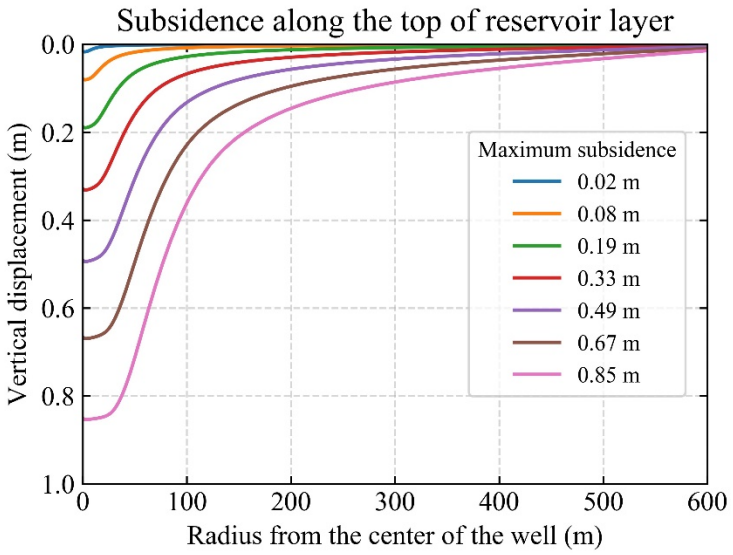

(b)

Figure 3 Simulated (a) pore pressure and (b) reservoir compaction profiles.

The reduced pore pressure distributions in the reservoir layer by depressurization is changed by assigning pore pressure distributions with two distinct radial zones explicitly: hydrate dissociated (high permeability) and undissociated (low permeability) zones. This is shown in Figure 3a. Using the coupled pore fluid-formation deformation analysis, the dissociated locations in the MH reservoir layer then compact by the increase in the effective stresses. The details about the modelling methodology of reservoir compaction are elaborated in Sasaki *et al.* (2019). The resultant reservoir subsidence profiles along the top boundary of the MH reservoir layer are shown in Figure 3b for different degrees of pore pressure reduction as shown in Figure 3a.

The behaviour of the wellbore (i.e., formation and cement) during the simulated reservoir subsidence is shown in Figure 4a. The axial displacements of the cement and formation both represent those along the cement-formation interface. It is shown that the displacements of the formation and cement increase in a similar fashion with increasing reservoir compaction. For example, the maximum axial displacement of approximately 500 mm is developed in both formation and cement at the bottom when the reservoir subsidence has also reached 500 mm at the wellbore location. It is noted, however, that the axial displacement of formation is slightly larger at the bottom and slightly smaller at the top than that of cement. As a result, the top and bottom areas of the interface develop relative displacement in the opposite directions (i.e., positive values in the top and negative values in the bottom) while the middle part is relatively unaffected. This interface behaviour is similar to shaft friction development between two pipes where the outer pipe is subjected to tensile loading. Therefore, in the following section, a theoretical analysis

of the shaft friction development of pipe-cement-pipe specimen under tensile loading is carried out in order to compare the behaviours of the specimen with those of the well simulated in the finite element analysis.

Figure 4b shows the replication of the wellbore deformation in the laboratory conditions, in which the wellbore is modelled by a well mode which consists of steel pipes and cement, and the axial deformation is induced by tensile loading. The detail of the well model and its analytical behaviour during tensile loading are presented in the following section, whereas the derivation of the analytical solution is provided in Appendix B.

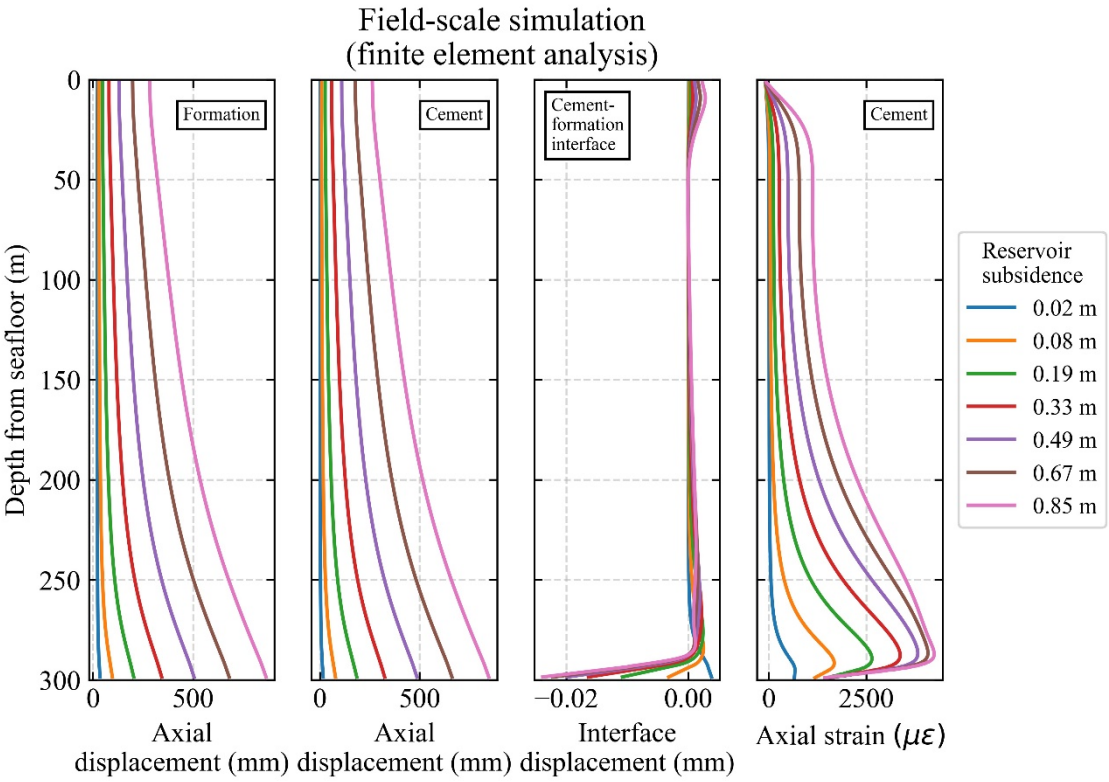

(a)

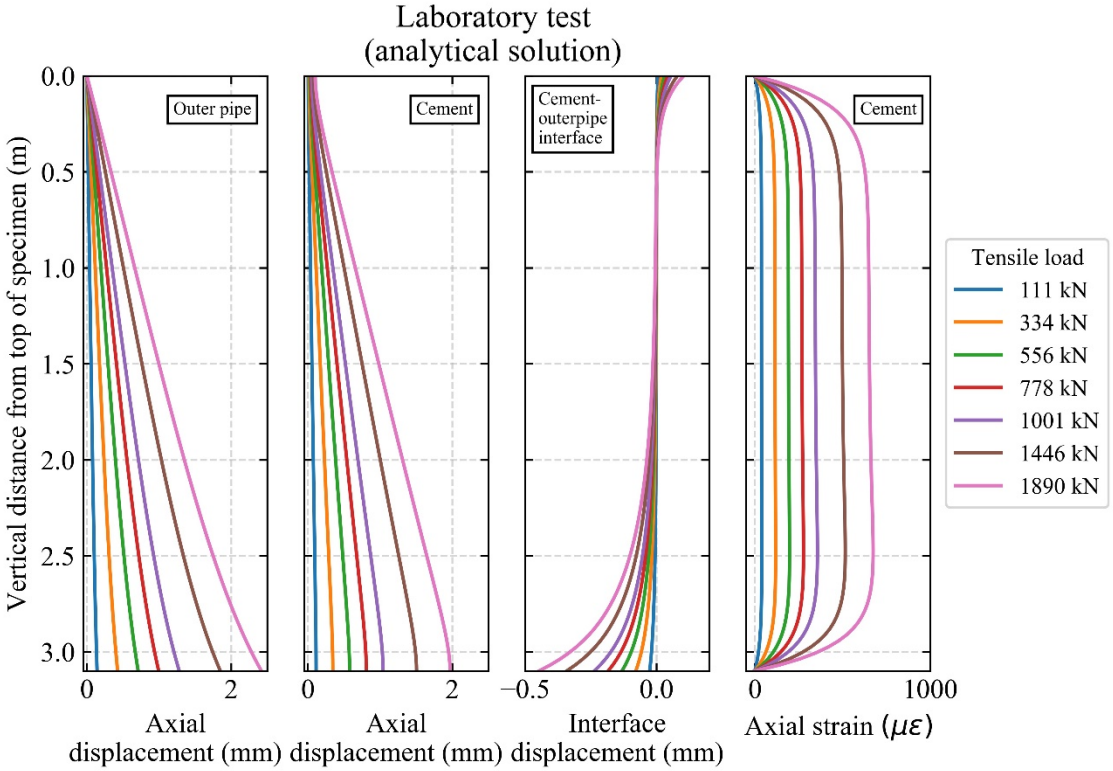

(b)

Figure 4 Behaviours of the well during reservoir compaction: (a) field-scale finite element simulation; (b) theoretical analysis in the laboratory condition.

2.2.2. Theoretical analysis of shaft friction development in a well model

A well model shown in Figure 5 is designed to simulate the axial tensile deformation of the well during reservoir compaction in the laboratory. The model consists of an inner pipe, cement and outer pipe. The outer pipe of the specimen is welded to the top and bottom plates while the inner pipe is welded only to the top plate. Hence, the application of tensile load via the top and bottom plates results in tensile strain development first in the outer pipe, which then propagates to the cement and to the inner pipe. The length of the specimen is 3.1 m (122 in.). The outer diameter of the inner pipe is 9 5/8 in. and the inner diameter of the outer pipe is 12 1/4 in., which are the same dimensions of a casing and borehole drilled in the Nankai Trough for the 2013 gas production test.

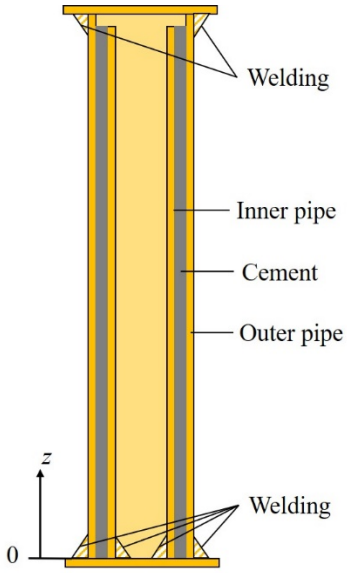

Figure 5 A schematic of the laboratory-scale well specimen.

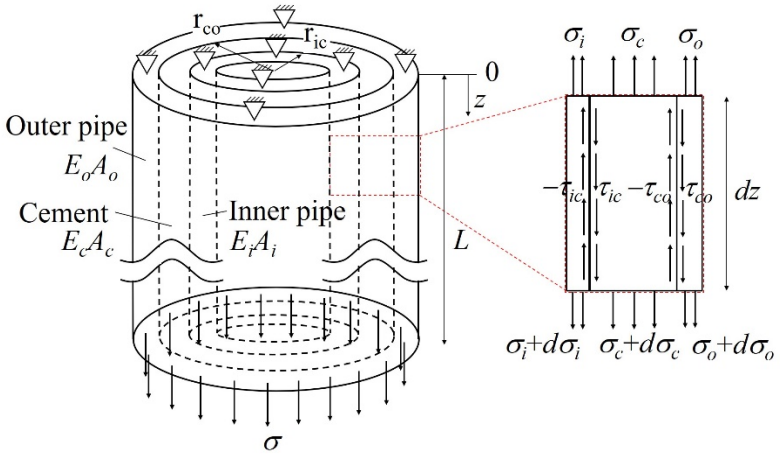

Figure 6 The assumed force equilibrium condition of the well specimen under tensile loading.

Figure 6 shows a schematic diagram of a segment of the well model under force equilibrium. It is noted that the well model (Figure 6) is shown upside down compared to the well specimen (Figure 5). The axial stress (σ) is applied at the bottom of the outer pipe while the displacement at the top of the outer and inner casing is constrained. The annular cement is constrained only by friction at the interface with the outer pipe. The inner pipe is not applied with any axial load at the bottom.

The derivation of the analytical solution of the well model behaviour is provided in Appendix B. The results of the theoretical analysis are shown in Figure 4b, in which the parameter values listed in Table 2 are used. The value of k is obtained by matching the well model predictions with the experimental results shown in the Discussion (Figure 17) section via trial and error The validity of the chosen value of k is further investigated through a finite element simulation of the tensile loading experiment (Sasaki *et al.*, 2019) and it is shown that the same value of k is obtained from it.

Table 2 Values of the parameters of the shaft friction model.

L (m)	3.1
E_o (GPa)	200
A_o (m^2)	6.334×10^{-3}
E_c (GPa)	8.3
A_c (m^2)	2.910×10^{-2}
E_i (GPa)	200
A_i (m^2)	7.031×10^{-3}
r_{co} (m)	0.1556
r_{ic} (m)	0.1222
k (GPa/m)	6.0
σ (MPa)	17.6, 52.7, 87.8, 122.9, 158.0, 228.2, 298.5

The behaviours of the specimen under tensile loading (Figure 4b) are qualitatively similar to those of the well during reservoir compaction simulated in the finite element analysis (Figure 4a). For example, positive and negative interface shear stress and displacement are developed in the top and bottom parts of the well model during tensile loading, respectively, which is the case in the well during reservoir compaction simulated in the finite element analysis. The negative values indicate that the outer pipe has displaced downward more than the cement. This is analogous to the overburden layer subsidence during reservoir compaction, which drags the well down. The absolute values of the interface shear stress/displacement between the laboratory and field conditions are, however, different. This is because of the difference in the cement-formation (finite element analysis) and cement-outer pipe (well model) interface properties: the latter is stiffer against interface shearing, which results in greater interface shear stress values (~ 2.5 MPa) than in the simulation (~ 1.0 MPa). Also, there are differences in the axial strain distribution: the axial strain reaches the maximum value at the bottom part of the well in the simulation whereas the peak value is developed in the middle zone in the theoretical model. This is because the reversal of the relative interface displacement direction in the simulation is developed in the bottom due to the Poisson's effect of the overburden layer, which displaces not only in the vertical but also in horizontal direction toward the well in response to reservoir subsidence. Finally, the

larger axial strain values in the simulation relative to the well model is developed due to the difference in the length of the well (300 m) and the well model (3.1 m): the longer the well is, the larger the surface area where interface shear force can develop to elongate the well. Other differences between the field-scale finite element simulation and laboratory-scale well model include, but are not limited to, the porous nature of the formation as oppose to solid steel that composes the outer pipe, geostatic confining stress gradient on the cement from the formation versus no confining stress in the well model, etc. Therefore, it is argued that the developed testing scheme of the well model to simulate the tensile deformation of the well is simple and feasible in laboratory conditions, but it is not a quantitative or exact modelling method of the field-scale tensile well deformation.

2.3. Monitoring of axial strain development of the well model

Distributed strain monitoring of the well model was conducted during the tensile loading. Distributed measurement techniques frequently employed in oil and gas wells are distributed fibre optic monitoring of temperature (Hurtig *et al.*, 1994; Großwig, Hurtig and Kühn, 1996; Williams *et al.*, 2000) and acoustic signals (Molenaar *et al.*, 2012; Hveding and Porturas, 2015; Thiruvenkatanathan *et al.*, 2016). For distributed fibre optic strain monitoring, a technique called Brillouin optical time domain reflectometry/analysis (BOTDR/A) (Horiguchi and Tateda, 1989; Horiguchi, Kurashima and Tateda, 1989; Horiguchi *et al.*, 1995) has been utilised in the oil and gas industry mainly for pipeline monitoring (Baldwin, 2015, 2018; Hveding, Bukhamsin and Aramco, 2018). This is because the advantage of BOTDR/A is considered to be the long measurement distance (i.e., ~ tens of kilometres). However, BOTDR/A is also applicable to the distributed strain monitoring of a well (Klar *et al.*, 2019). In the construction industry, BOTDR/A has been used for the deformation monitoring of pile foundations (Klar *et al.*, 2006; Bourne-Webb *et al.*, 2009; Mohamad *et al.*, 2011; Pelecanos *et al.*, 2017, 2018). Although monitoring of a pile is analogous to monitoring of a well, the lengths are significantly different: the latter is much deeper (up to 10,000 m) than the former (up to 100 m). As a result, a well is subjected to larger deformation in deep geologic strata such as fault slip than a pile. In this study, BOTDR/A was employed to conduct distributed strain monitoring of the well model during the tensile loading so as to investigate the potential of BOTDR/A to carry out well integrity monitoring in the field.

A schematic diagram of the principal of the BOTDR measurement is illustrated in Figure 7. The analyser measures the frequency component of the backscattered light pulses and the shift in the frequency is correlated with strain and/or temperature change applied to the fibre. For further details of the BOTDR measurement, relevant literatures such as (Horiguchi and Tateda, 1989; Horiguchi, Kurashima and Tateda, 1989; Horiguchi *et al.*, 1995; Hotate and Hasegawa, 2000; Li

et al., 2017) should be consulted. The frequency shift is linearly proportional to strain and/or temperature change, as shown in Equation 1:

$$\Delta\nu_B = C_\epsilon \Delta\epsilon + C_T \Delta T \quad (1)$$

where $\Delta\nu_B$ = Brillouin frequency shift (MHz); $\Delta\epsilon$ = change in strain (με); ΔT = change in temperature (°C); C_ϵ = strain coefficient (MHz/ με); C_T = temperature coefficient (MHz/ °C). It is noted that the BOTDA measurement is identical to BOTDR measurement except that the measurement error and accuracy are improved in BOTDA by shooting another light pulses from the other end of the optical fibre (Horiguchi and Tateda, 1989; Horiguchi, Kurashima and Tateda, 1989). As a result, for BOTDA, both ends of the optical fibre have to be connected to the analyser to obtain strain profiles. On the other hand, BOTDR requires only one end of the optical fibre to be connected to the analyser.

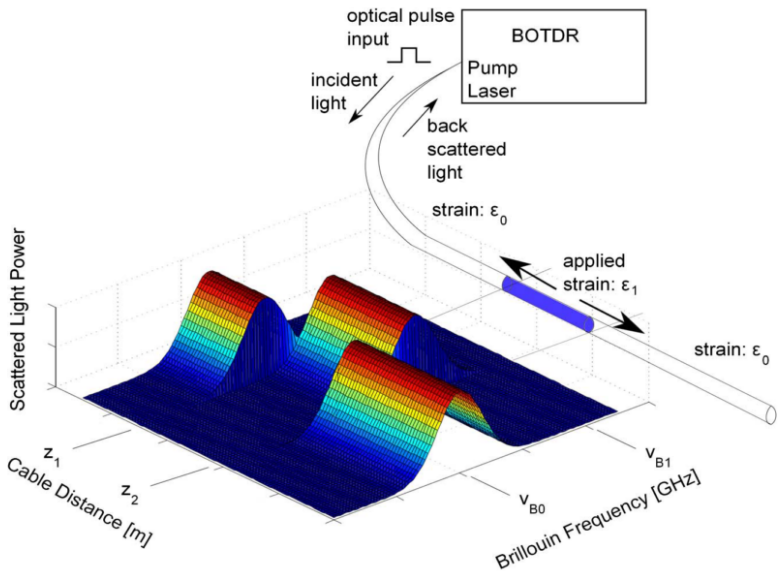

Figure 7 The principle of the BOTDR measurement [after (Pelecanos *et al.*, 2017)].

In addition to BOTDR/A, Real-Time Compaction Imager (Pearce and Legrand, 2009; Pearce and Rambow, 2009; Earles *et al.*, 2010) was applied to the well model. It utilizes a special optical fibre inscribed with fibre Bragg grating (FBG). A fraction of the light shot into the fibre is reflected at the gratings. The shift in the wavelength of the reflected light is linearly related to changes in strain and temperature along the optical fibre as shown in Equation 2:

$$\Delta\lambda' / \lambda_0 = (1 - p_e)\Delta\epsilon + (\alpha_n + \alpha_L)\Delta T \quad (2)$$

where $\Delta\lambda'$ = change in wavelength of the reflected light (nm); λ_0 = baseline wavelength of the reflected light (nm); $\Delta\epsilon$ = change in strain (με); ΔT = change in temperature (°C); p_e = effective photo-elastic coefficient (1/ με); α_n = thermo-optic coefficient (1/ °C); α_L = linear thermal expansion coefficient (1/ °C). The FBG measurement is made at discrete grating locations which are placed every 2 cm along the fibre for 250 m length. Similar to BOTDR, the FBG measurement needs only one end of the optical fibre to be connected to the analyser to take measurements.

As shown in Equation 1 and 2, the frequency/wavelength shift in the BOTDR/A and FBG measurements is affected by both strain and temperature changes. Hence, the temperature term has to be compensated for to extract strain changes from the measurement data. This can be performed by installing a temperature fibre optic cable, in which the fibre core is encased in an air- or gel-filled tube which isolates the fibre core from external strains, alongside a strain fibre optic cable, where the fibre core is tightly buffered to the coating layers of the cable. As a result, the entire frequency/wavelength shift measured along the temperature cable is converted into temperature change (i.e., $\Delta T = \Delta\nu_B/C_T$ for BOTDR/A and $\Delta T = (\Delta\lambda' / \lambda_0)/(\alpha_n + \alpha_L)$ for FBG). This temperature change is then used to calculate the temperature term in the measurement data obtained along the strain cable to extract strain changes.

Also, it is noteworthy that the primary difference between the BOTDR/A and FBG measurements is that the former measures an average strain value over a certain gauge length along the optical fibre (i.e., spatial resolution), whereas the latter measures local strain values like traditional strain gauges. For BOTDR/A, the spatial resolution is dependent on the performance of the analysers employed for the measurement and it is typically 0.5 m and 1.0 m for BOTDA and BOTDR analysers, respectively. The spatial resolution of FBG is 5 mm, which is the length of the grating. The data sampling interval and measurement distance are also different between the BOTDR/A and FBG techniques. The data sampling interval of BOTDR/A measurements can be adjusted depending on acceptable data acquisition speed for specific applications but it may in general vary between a few centimetres and few metres. Ordinary FBG measurements, on the other hand, have a larger sampling interval. This is because the number of FBG gratings that can be inscribed on a single optical cable is limited to ~ 30 gratings due to the power loss of light at gratings by reflection. The special FBG technique employed in this study, however, is capable of using optical fibres in which several thousands of gratings are inscribed. As a result, the sampling interval of the FBG technique employed in this study is 2 cm. The drawback of this FBG technique is that the measurement distance is limited to below 250 m, whereas BOTDR/A can measure greater

than several tens of kilometres.

The primary measurement characteristics of the two analysers are provided in Table 3. The spatial resolution and sampling interval are both finer in the FBG than in the BOTDR. However, this comes at a cost of the relatively short measurement distance for the FBG: 250 m maximum measurement length per channel compared to 45 km for the BOTDR. Therefore, the FBG technique may be suitable for the monitoring of specific sections of the well (e.g., reservoir interval), whereas BOTDR can cover the rest of the well length.

Table 3 The primary measurement characteristics of the Omnisens and FBG analysers.

	Spatial resolution (m)	Data sampling interval (m)	Axial strain measurement precision (με)	Maximum fibre length per channel (km)	Measurement duration per channel (min)
Omnisens (Omnisens, 2019)	1	0.25	20–60	45	5–15
FBG (Baker Hughes, 2019)	0.005	0.02	10	0.25	3.5

3. Well model preparation

3.1. Configuration

Figure 8 shows the cross sections of the well model. The outer diameter of the inner pipe is 9 5/8 in. (0.24 m) and the inner diameter of the outer pipe is 12 1/4 in. (0.31 m). These dimensions correspond to the diameters of a casing and borehole deployed at the Nankai Trough (Yamamoto *et al.*, 2014). The height of the model is 3.1 m (122 in.), which is about three times the spatial resolution of the BOTDR measurement by the Omnisens analyser (1.0 m). To prepare the well model, the inner and outer pipe subassemblies are fabricated separately (Figure 9) and they are assembled in the laboratory while installing fibre optic cables in the specimen annulus.

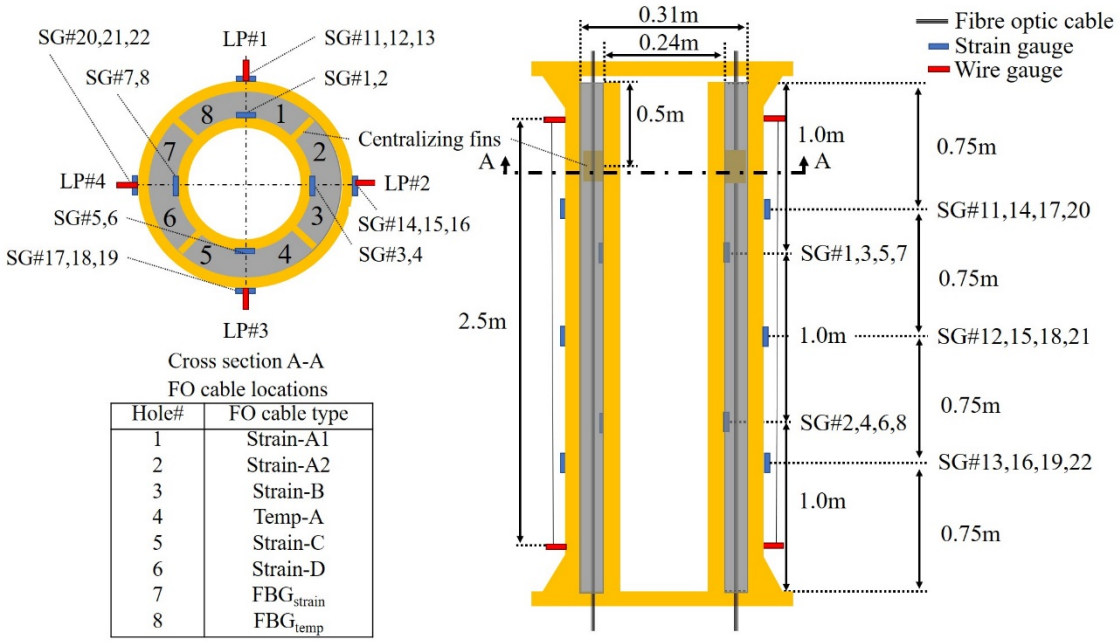

FO cable locations

Hole#	FO cable type
1	Strain-A1
2	Strain-A2
3	Strain-B
4	Temp-A
5	Strain-C
6	Strain-D
7	FBG_{strain}
8	FBG_{temp}

Figure 8 The cross sections of the well specimen with types and locations of the instrumented sensors.

Figure 9 The inner pipe (left) and outer pipe (right) subassemblies of the well specimen.

3.2. Sensor installation

The types, locations and number of the sensors instrumented to the model are also shown in

Figure 8. Eight strain gauges are attached to the inner pipe, whereas twelve strain gauges are attached to the outer pipe. Wire gauges, which consist of piano wires attached to position transducers, are also instrumented on the outer pipe for average strain measurement.

The fibre optic cables for the BOTDR measurement are run through Hole #1 to #6 in the specimen annulus. The cables are then spliced to form a single fibre optic cable as shown in Figure 10. The FBG cables are installed in Hole # 7 and #8 and they are not spliced with the other cables.

The cross sections of the fibre optic cables employed for the BOTDR and FBG measurements are shown in Figure 11. The cable characteristics vary significantly in terms of their coating layers. For example, the Strain-B cable has multiple (excessive) coating layers which make it robust enough to survive the field installation process. However, the strain sensitivity of this cable is expected to be limited due to increased potential of slippage of the coating layers relative to each other. The Strain-A1, -A2, -C and -D cables, in contrast, have simpler cross-sections than the Strain-B cable, which makes these cables strain-sensitive but vulnerable to damage. There is a trade-off between robustness and strain sensitivity of fibre optic cables. The FBG cable, which is provided by Baker Hughes, consists of a stainless inner rod and outer tube. Two optical fibres are installed in the gap between the inner rod and outer tube by an adhesive. The fibres follow a helical path and that allows each individual cable to measure its own bend separate from axial strain. Also, the cable demonstrates 100% strain locking from the fibre to the outer sheath up to and beyond 2% strain, which is challenging for any of these other fibre optic cables examined in this experiment. The Temp-A cable is for temperature measurement as the optical fibres in this cable are encased in a gel-filled tube which isolates the fibres from external strains. The values of the strain and temperature coefficients of the fibre optic cables employed in the experiment are listed in Table 4 and Table 5.

During the experiments, fibre breakage was detected in the fibre optic cable loop during model preparation (between Hole #3 and #4 in Figure 10) and it was not possible to fix it within the timeframe of the experiment. Therefore, BOTDR was employed to take measurements because the two ends of the fibre cable were not accessible to perform BOTDA.

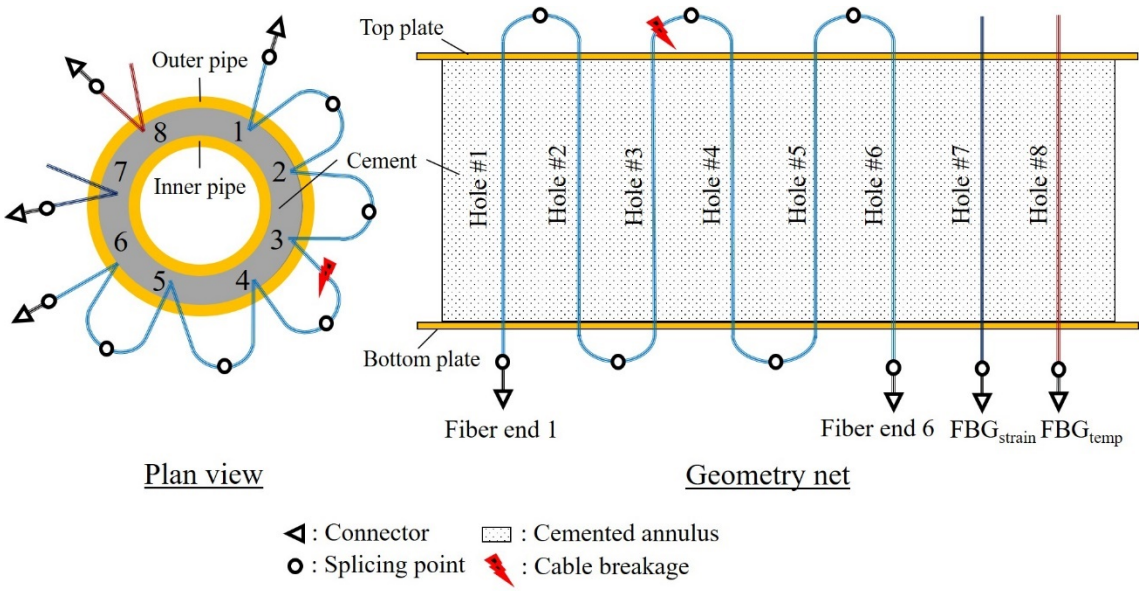

Figure 10 The configuration of the fibre optic cables installed in the specimen.

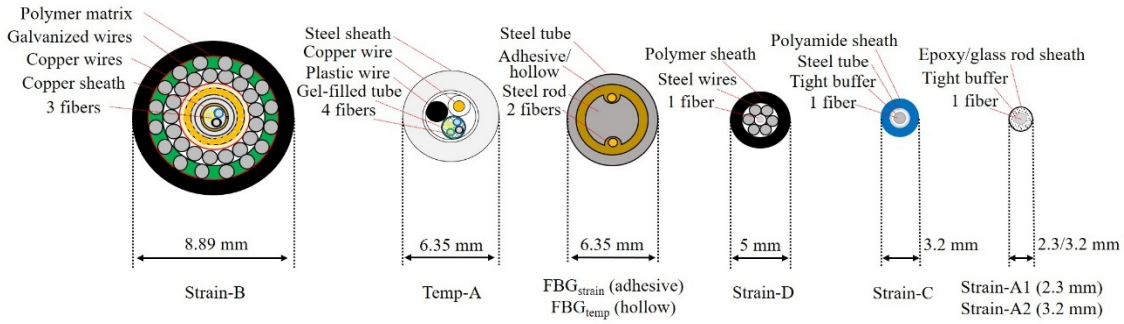

Figure 11 The cross sections of the fibre optic cables.

Table 4 Values of the strain and temperature coefficients of the BOTDR cables.

	Strain coefficient, C_ε (MHz/%)	Temperature coefficient, C_T (MHz/°C)
Strain-A1	468	1.03
Strain-A2	468	1.03
Strain-B	500	1
Strain-C	450	1.1
Strain-D	499.8	1.775
Temp-A	N/A	1

Table 5 Values of the strain and temperature coefficient of the FBG cables.

	Strain coefficient, 1 - p_e (1/με)	Temperature coefficient, $\alpha_n + \alpha_L$ (1/°C)
FBG_{strain}	0.7874×10^{-6}	19.05×10^{-6}
FBG_{temp}	0.7874×10^{-6}	9.15×10^{-6}

3.3. Monitoring of cement cure process

Class G cement, water and shrinkage reducing admixture (ASTM C494 Type S) was mixed together to prepare cement slurry. The water-to-cement ratio was set to 0.44 and the ratio of the shrinkage reducing admixture was set to 0.75% of the volume of the slurry. The mixing was carried out in four separate batches. The entire cement pour was completed in approximately an hour, after which BOTDR and FBG measurements were initiated to monitor the temperature change of the cement slurry during its curing process. The baseline BOTDR and FBG measurements were taken prior to the cement pour.

Figure 12a and b show the temperature change in the annular cement during its curing period measured along the Temp-A cable (BOTDR) and FBG_{temp} cable (FBG), respectively. The different measurement timings between the BOTDR and FBG analysers are due to different automatic measurement settings in each analyser. Regardless of that, the averaged nature of the BOTDR measurement relative to the FBG measurement is captured in the temperature distributions, as the FBG measurement detects localized high temperature zone between 0 m to 1.0 m (> 16.3 h), whereas it is averaged out in the BOTDR measurement. For example, the average temperature between 0 and 1.0 m is approximately 10ºC higher than that between 1.0 and 3.0 m at 21.4 h in the FBG measurement (i.e., the brown line in Figure 12). This is because the first batch of slurry was diluted by the insufficiently mixed second batch when it was poured into the specimen annulus. Insufficient mixing resulted in subdued cement hydration reaction and hence the lower heat emission. As a result, the low temperature zone ranges over the entire bottom half of the specimen (i.e., 1.0 m to 3.0 m). The subsequent third and fourth batches did not dilute the preceding slurry in the annulus due probably to their slightly lighter unit weight, as cement particles are evenly dispersed in water in these slurry batches, than the preceding batches. The temperature distributions measured by BOTDR did not capture the localized high temperature zone because of the spatial resolution of the BOTDR measurement (i.e., 1 m), over which the actual measurand distribution is convoluted with a Gaussian or Lorentzian function. The FBG measurement was able to detect it due to densely distributed gratings along the FBG cable. It is noted that the temperature increase in the annulus up to 10.4 h is relatively uniform over the specimen length, indicating that the high temperature zone is not caused by the time lag between the pouring of the four separate slurry batches (~ 15 min per batch). Also, it may be noteworthy that the insufficiently mixed part of the cement might behave differently from the sufficiently mixed part during tensile loading due to the differences in their stiffness and strength. However, this was not the case as the measured strain distributions of the cement were uniform over the entire specimen length, which is presented in the next section.

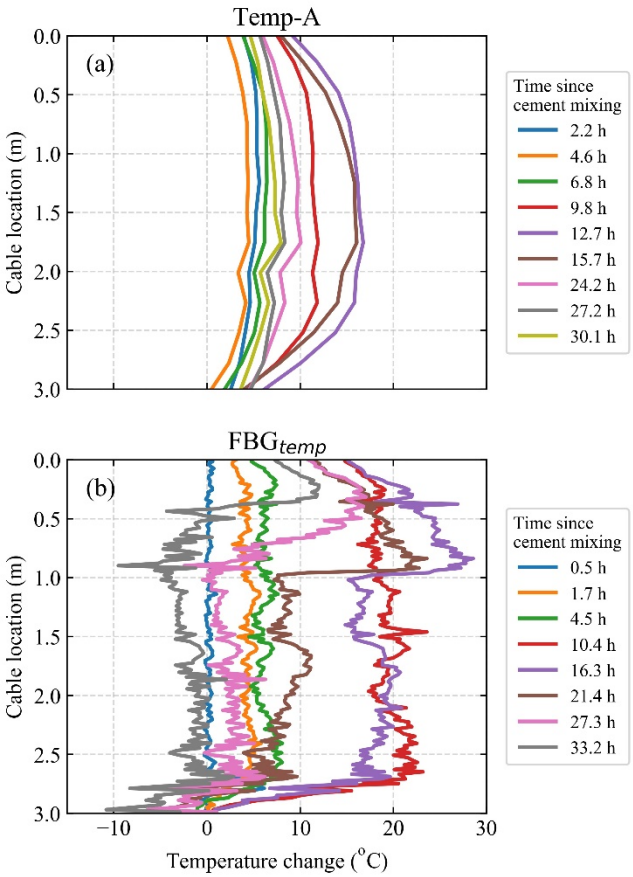

Figure 12 Temperature change in the cement during its curing period: (a) BOTDR measurement; (b) FBG measurement.

4. Tensile loading experiment

4.1. Loading scheme

Six days after the start of cement pouring, the tensile loading test was carried out. Figure 13 shows the well model set up in a loading apparatus at the Richmond Field Station facility of the University of California, Berkeley. Figure 14 shows the time series of the load increments as well as the ambient temperature change during the loading test. Each load increment was held for approximately 15 min to take BOTDR and FBG measurements. Cyclic loading was carried out between 111 kN and 778 kN (i.e., between 1 h and 3 h in Figure 14) to assess potential hysteresis in the strain sensitivity of the fibre optic cables. After the cyclic loading, the load was increased monotonically until the specimen failed in the top part of the outer pipe as shown in Figure 15.

Figure 13 The well specimen set up in a loading frame after cement cure.

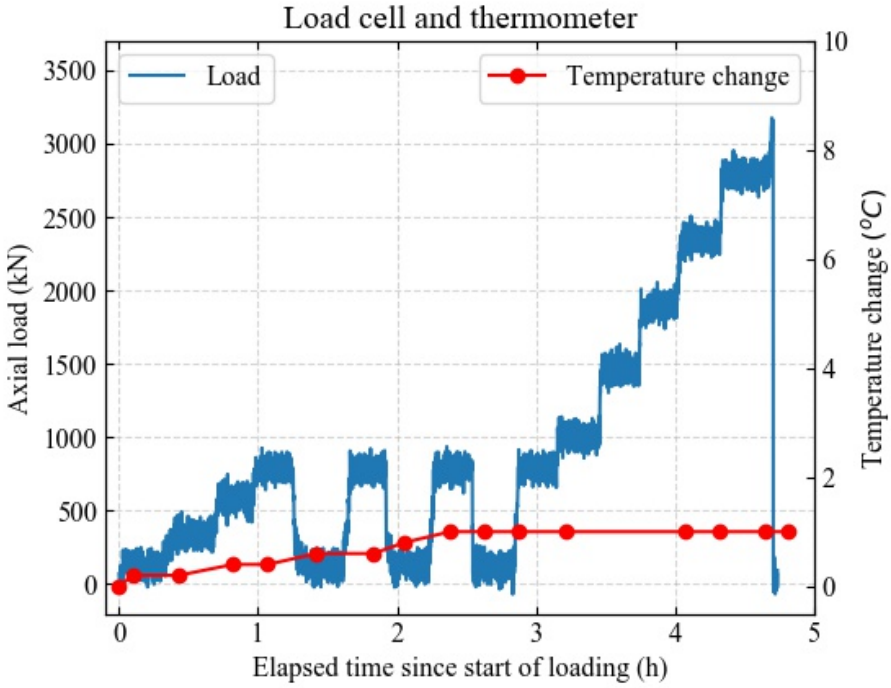

Figure 14 The time series of the tensile axial load and temperature change during the loading test.

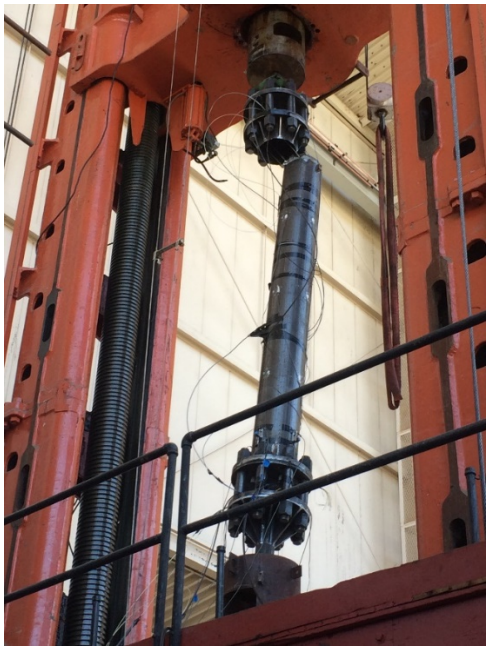

Figure 15 Failure of the specimen in the top part of the outer pipe.

4.2. BOTDR and FBG measurement results

Figure 16 shows the result of the BOTDR and FBG measurements. It is found as expected that the FBG measurement is able to capture localised strain changes (as opposed to averaged strain changes by the BOTDR measurement). It is assumed in this study that the FBG strain profiles are the actual strain profiles of the model under loading and the FBG strain profiles are thus used for the performance evaluation of the fibre optic cables employed for the BOTDR measurement.

Figure 16a and b show the BOTDR strain profiles along the Strain-A1 and Strain-A2 cables, respectively. These strain profiles are similar to each other despite the difference in the diameter of these cables (i.e., 2.3 mm for Strain-A1 and 3.2 mm for Strain-A2). The maximum strain magnitude obtained along the Strain-A cables is approximately 1200 με at 2,780 kN, which compares favourably with the value obtained along the FBG_{strain} cable (i.e., roughly 1100 με at 2,780 kN). No strain hysteresis is observed in the Strain-A1 and -A2 cables during the cyclic loading.

Figure 16c shows the BOTDR strain profiles obtained along the Strain-B cable. The measured strain magnitudes are slightly smaller than those obtained along the Strain-A cables and FBG_{strain} cable. Also, the strain distributions are not symmetric. This is because of ineffective strain transfer in the coating layers of the Strain-B cable as the number of coating layers is

excessive relative to that of the Strain-A cables as shown in Figure 11.

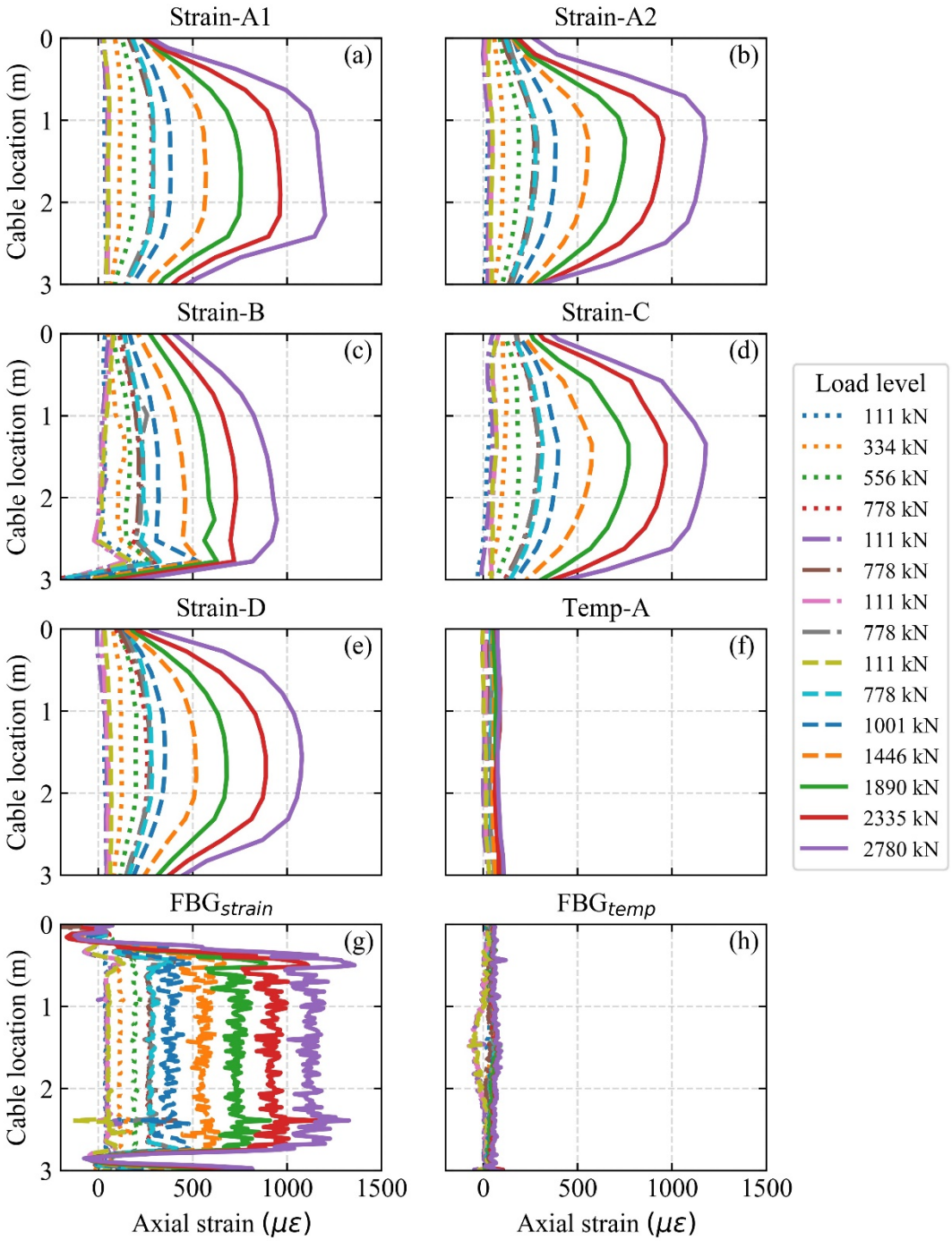

Figure 16 Axial strain profiles obtained from the BOTDR and FBG measurements: (a) Strain-A1 (BOTDR); (b) Strain-A2 (BOTDR); (c) Strain-B (BOTDR); (d) Strain-C (BOTDR); (e) Strain-D (BOTDR); (f) Temp-A (BOTDR); (g) FBG_{strain} (FBG); (h) FBG_{temp} (FBG).

Figure 16d and e show the BOTDR strain profiles along the Strain-C and Strain-D cables, respectively. Both profiles are symmetric with the peak strain measured at the mid-length of the specimen (~ 1.5 m). However, the maximum strain magnitudes at each load increment are larger in the Strain-C cable than in the Strain-D cable. This is mainly because the coating layers of the Strain-C cable are tightly buffered by mechanical compression and chemical adhesion, whereas the Strain-D cable relies only on the mechanical compression through the steel wires which may be prone to slippage. As a result, slippage in the coating layers might have occurred during the cyclic loading period in the Strain-D cable. The result suggests the importance of tightly buffered coating layers to achieve sufficient strain sensitivity.

It is noted that no axial strain development is detected along the Temp-A and FBG_{temp} cables (Figure 16f and h) as the optical fibres in these cables are isolated form external strains in the gel- and air-filled tubes encased in the respective cables.

5. Discussion

5.1. Shaft friction analysis of the specimen

Figure 17 shows the analytical axial strain distributions of the inner casing, cement and outer pipe obtained from Equation B6 presented earlier, which are compared with the strain distributions obtained from the strain gauges and FBG cable. The values of the parameters used in the equations are listed earlier in Table 2. It is found that the match between the analytical and experimental axial strain distributions is satisfactory. The minimum and maximum errors of the analytical solution relative to the experiment range between 1.65% (556 kN) and 12.2% (2780 kN) for the inner pipe at the two strain gauge locations, between 0.389% (556 kN) and 8.90% (2780 kN) for the cement at the middle height of the specimen and between 0.311% (111 kN) and 14.8% (2780 kN) for the outer pipe at the three strain gauge locations. This proves that the theoretical concept of the tensile axial deformation of the well model is properly implemented in the design of the specimen and loading scheme. This shaft friction analysis has thus verified that the axial tensile deformation of the well is simulated successfully in the laboratory.

The errors between the analytical and experimental strain values in the cement after 1001 kN are perhaps caused by plastic deformation of the specimen. In fact, the strain distributions of the FBG cables start to oscillate from this load level. Other causes such as the heterogeneity of the cement column (sufficiently vs. insufficiently mixed cement parts) and presence of cement defects (void, micro annulus, etc.) may also be responsible for the errors. Since the strain distributions of the

FBG and other fibre optic cables show larger values than the analytical strain distributions, potential fibre optic cable slippage at the interface between the cables and cement and/or between the fibre core and its coating layers is not induced within the strain range examined in this experiment (~ 1,250 με).

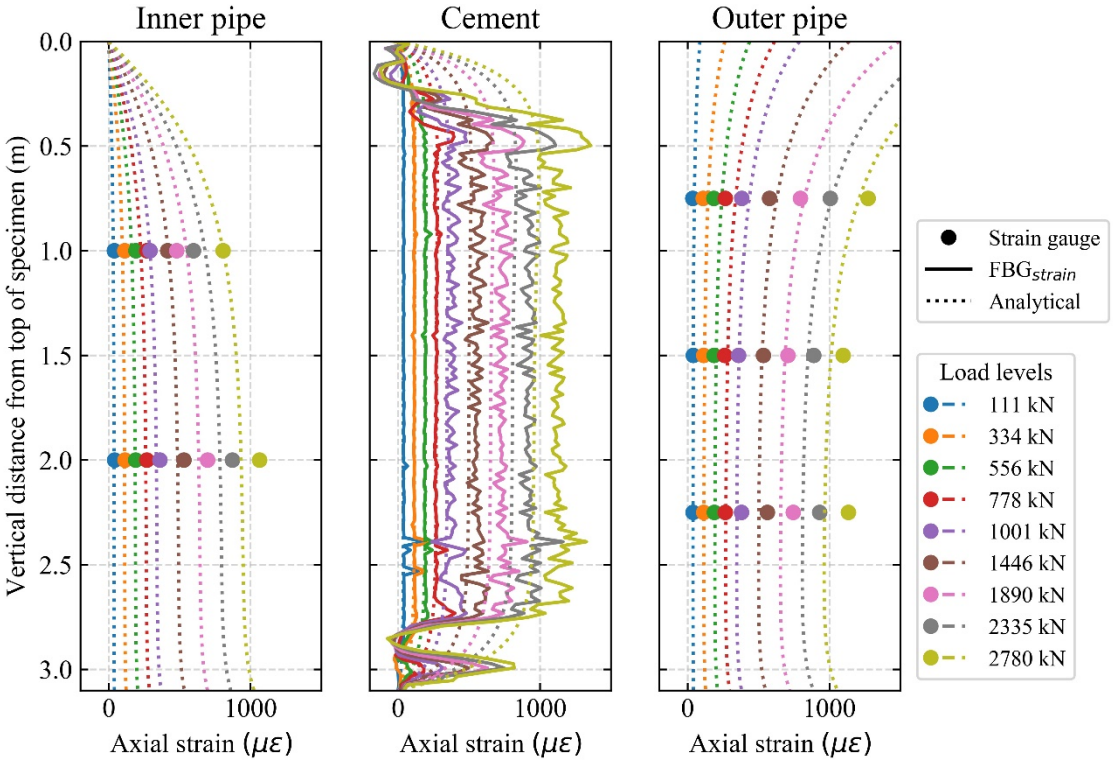

Figure 17 Comparison between the analytical (dotted lines) and experimental (solid lines and solid dots) axial strain distributions of the specimen.

5.2. Comparison between BOTDR and FBG measurements

The BOTDR strain profiles are calculated as the convolution of the real strain profile (ε_{real}) with a Gaussian or Lorentzian function. In this study, the Gaussian function as shown in Equation 3 is employed to calculate pseudo BOTDR strain profiles:

$$\epsilon_{BOTDR}(x) = \epsilon_{real}(x) * \frac{1}{\sqrt{2\pi\sigma_G^2}} e^{-\left(\frac{x^2}{2\sigma_G^2}\right)} = \int_{-\infty}^{\infty} \epsilon_{real}(\tau) \frac{1}{\sqrt{2\pi\sigma_G^2}} e^{-\left(\frac{(x-\tau)^2}{2\sigma_G^2}\right)} d\tau \quad (3)$$

where x = cable distance; $\epsilon_{BOTDR}(x)$ = pseudo BOTDR strain profile; $\epsilon_{real}(x)$ = real strain profile; σ_G = standard deviation of the Gaussian distribution.

The spatial resolution of the BOTDR measurement is defined as the full width at half maximum (FWHM) of the frequency–power spectrum of the incident light pulse, which is assumed to follow the Gaussian distribution herein. The FWHM of the Gaussian distribution is equal to 2.35σ. This is obtained by solving the equation $1/2\sqrt{2\pi\sigma_G^2} = e^{-x^2/2\sigma_G^2}/\sqrt{2\pi\sigma_G^2}$ for x, i.e., $2x$ (full width at half the peak value of the Gaussian distribution) is calculated to be $2.35\sigma_G$. Hence, equating it with the spatial resolution of the BOTDR measurement (i.e., 1.0 m) yields σ_G = 0.424 m. This value of the standard deviation is used in Equation 3 to turn the FBG strain profiles, which are assumed to be the real strain profiles, ε_{real}, to generate pseudo BOTDR profiles. The pseudo BOTDR strain profiles are then compared with the actual BOTDR strain profiles measured along the fibre optic cables (i.e., Strain-A1, -A2, -B, -C and -D cables) to evaluate their strain sensing performances.

The comparison between pseudo and actual BOTDR strain profiles are shown in Figure 18. It is found that the pseudo and actual BOTDR strain profiles are in good agreement, which shows that the strain sensitivity of the fibre optic cables employed for the BOTDR measurement is sufficient. The exception, however, is the Strain-B cable as is mentioned earlier due to the excessive number of coating layers, which highlights the necessity to simplify the coating layers of this cable. Applying mechanical compression and/or chemical adhesion between the coating layers might improve the strain sensitivity of the Strain-B cable.

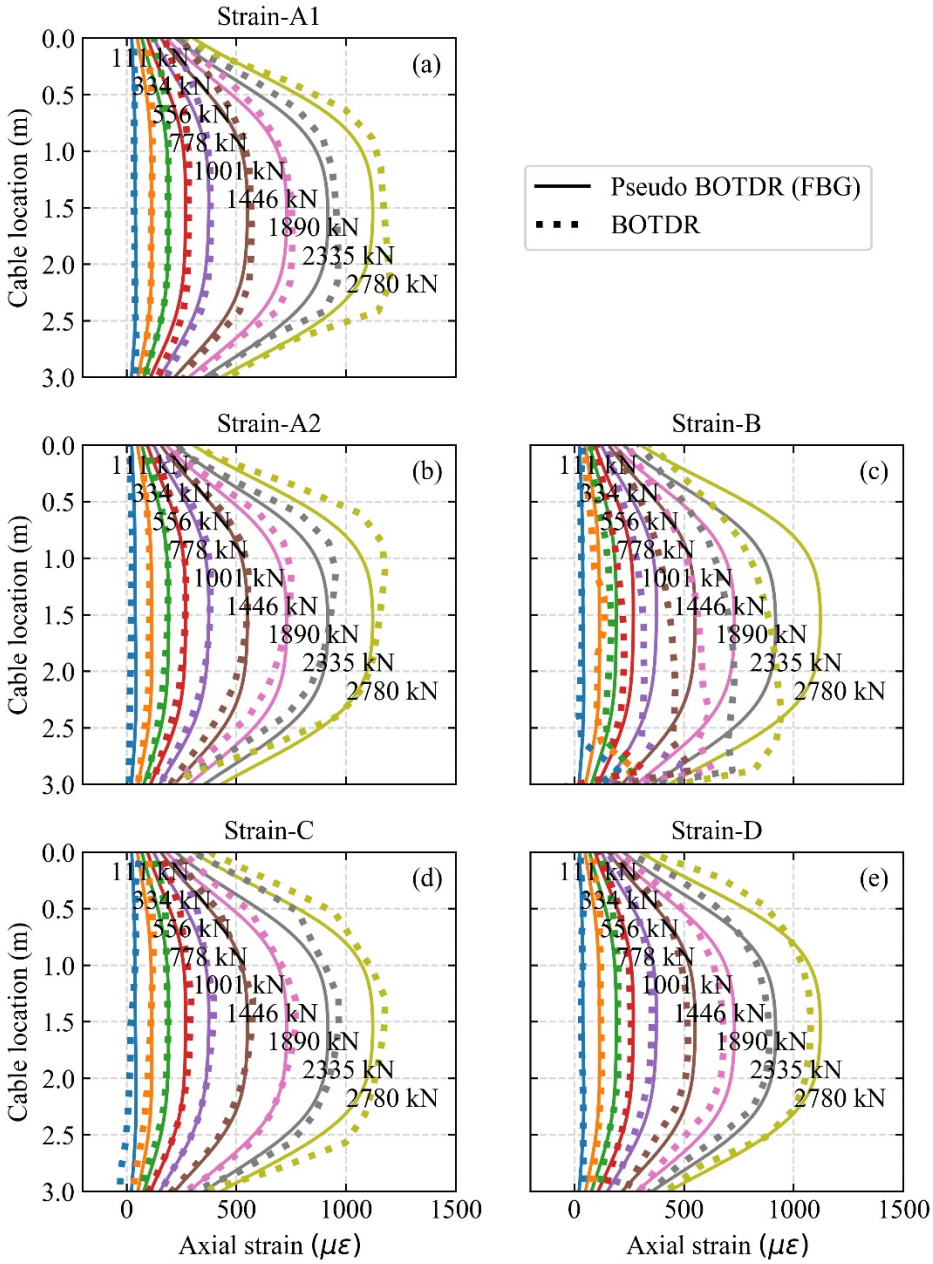

Figure 18 Comparison between the strain profiles calculated by the convolution of the FBG strain profiles with the Gaussian function (i.e., solid lines) and the actual BOTDR strain profiles (i.e., dashed lines): (a) Strain-A1; (b) Strain-A2; (c) Strain-B; (d) Strain-C; (e) Strain-D.

5.3. Comparison between fibre optic and strain gauge measurements

Figure 19 shows the comparison between the fibre optic (i.e., BOTDR and FBG) and strain gauge measurements. BOTDR and FBG strain measurement data are extracted at approximately the mid-height of the specimen (~ 1.5m). Hence, the strain gauges located near the mid-height of the specimen are selected for comparison.

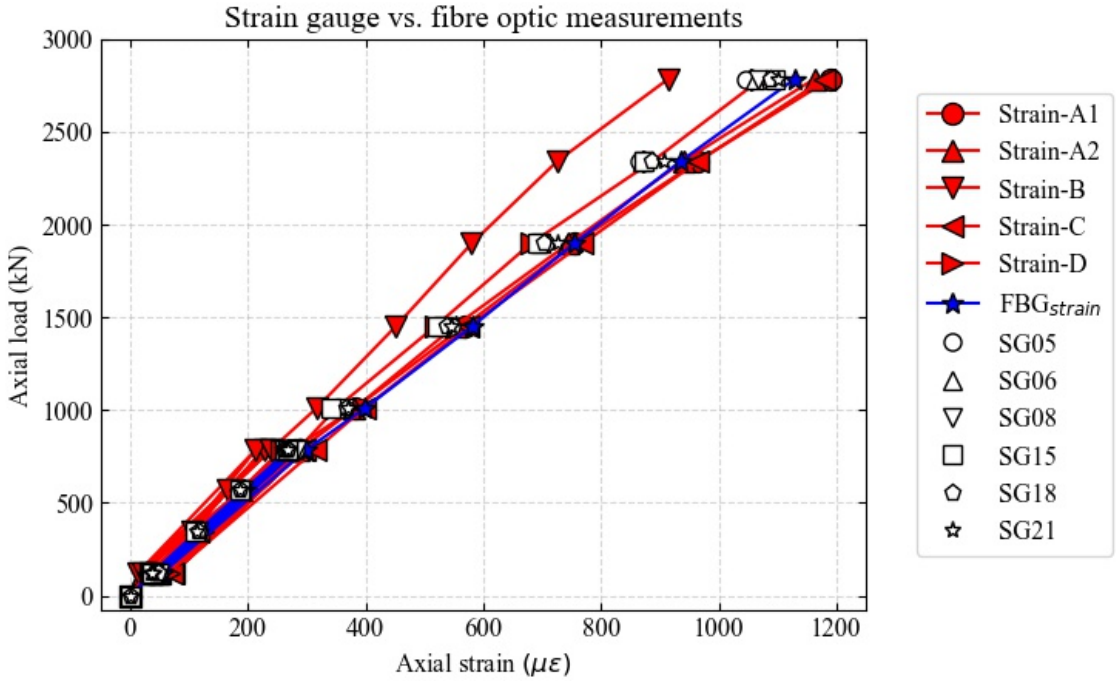

Figure 19 Comparison between the fibre optic and strain gauge measurements.

It is found that the BOTDR and FBG measurements are in good agreement with the strain gauge measurements. The average error of the FBG measurement relative to the average strain gauge measurement is 7.73%, whereas that of the BOTDR measurement is 8.85% (Strain-A1), 9.11% (Strain-A2), 18.9% (Strain-C) and 10.3% (Strain-D). It is noted that the average error of the Strain-C cable is apparently large because the absolute error of this cable at the smallest load levels in the experiment (three points of 111 kN during cyclic loading) is large. The average error of the Strain-C cable in the other load levels is 9.90%. However, there are large differences between the strain values obtained from the Strain-B cable and the other cables/strain gauges. The average measurement error in the Strain-B cable relative to the strain gauge measurement is 20.8%, which is more than twice as large as that of the FBG and BOTDR measurements in the other cables provided above (without the data points at 111 kN, the average error in the Strain-B cable is 14.5%). The difference is again attributed to the ineffective strain transfer in the Strain-B cable as the coating layers of this cable are not tightly buffered through mechanical compression or chemical adhesion, in addition to the excessive number of coating layers. Therefore, it is argued that key to accurate strain monitoring with BOTDR/A is to employ fibre optic cables with a simple yet robust cross-sectional structure with a small number of coating layers that are tightly buffered to each other. One way to achieve such fibre optic cables is to encase an existing tightly buffered strain cable such as the Strain-C cable in a metal tube and fill

the gap with a filler material. The filler material should be chosen such that it does not develop excessive or localized deformation in response to external strains as it hinders effective strain transfer to the optical fibres.

6. Conclusions

In this research, a methodology to simulate the axial tensile deformation of a well during reservoir compaction in a laboratory-scale loading test is developed. The mechanism of the axial tensile well deformation is analysed in a finite element analysis where reservoir compaction is simulated and the well behaviour is found to be qualitatively equivalent to that of a concentric double pipe specimen subjected to tensile loading. In order to validate the developed well integrity testing methodology, a tensile loading test is performed on a well specimen which consists of an inner pipe, cement sheath and outer pipe. Distributed fibre optic strain monitoring techniques (BOTDR and FBG) are employed to measure the distributed strain profiles of the well specimen under tensile loading, so that the design concept of the specimen and loading scheme can be confirmed to follow the theoretical predictions. Finally, the feasibility of performing distributed strain sensing of well integrity with BOTDR is assessed in the tensile loading experiment with an emphasis on the effect of the characteristics of fibre optic cables on the strain measurement accuracy. Results from this study have yielded the following findings:

(i) The field-scale finite element simulation on well integrity during reservoir compaction computed the vertical distributions of axial displacement, interface relative displacement and axial strain in the cement sheath and formation which are found to be qualitatively similar to those of a laboratory-scale well model subjected to tensile loading. The proposed design of the well specimen and loading scheme are verified in a laboratory tensile loading test where measured axial strain distributions of the specimen are found to follow those calculated by the analytical solution. Therefore, a methodology to simulate the axial tensile deformation of the well during reservoir compaction in the laboratory has been established.

(ii) BOTDR is found to be effective in measuring the axial tensile deformation of the well in the tensile loading experiment of the well specimen. Within the limitation of the spatial resolution of the BOTDR measurement (1.0 m), BOTDR has provided accurate axial strain distributions of the well specimen at different tensile load increments. The BOTDR measurement results are validated by the FBG measurement.

(iii) In order to ensure the accuracy of the BOTDR measurement, it is found to be critical for fibre optic cables used with BOTDR to have the following characteristics: tight-buffered coating layers around the optical fibre cores via mechanical compression and/or chemical adhesion, and a small number of coating layers.

Further research is necessary to identify a robust and effective fibre optic cable for the in-well strain measurement with BOTDR. The developed tensing method will be a simple and cost-effective means to test existing and newly developed fibre optic cables against tensile well deformation. Once a suitable fibre optic cable is identified in the laboratory, the cable can be installed in the field behind casing prior to its being lowered into the borehole and the cable is then cemented in the annulus. Strain profiles of the well are obtained by carrying out periodic BOTDR measurements and they can be used to detect highly strained regions of the well during oil/gas production process. This will enable early warning of potential well damage/failure to facilitate timely countermeasures. Also, numerical simulators for reservoir geomechanics can be calibrated using BOTDR strain profiles to increase the accuracy of such numerical simulation. An accurate estimation of the formation deformation will become possible in this manner, which is key to assessing the environmental impact and safety of oil/gas production from methane hydrate and other conventional hydrocarbon reservoirs.

Appendix A: SI-imperial unit conversion table

Table A1 SI-imperial unit conversion.

	SI units	Imperial units
Force	1 kN	0.2248 kips
Stress	1 MPa	145.038 psi
Displacement	1 m	39.3701 inches

Appendix B: Analytical solution of the well model behaviour

The force equilibrium equations for the outer pipe, cement and inner pipe as shown in Figure 6 are as follows:

$$\begin{cases} E_o A_o \dfrac{\partial^2 y_o}{\partial z^2} + 2\pi r_{co} k(y_c - y_o) = 0 \\ E_c A_c \dfrac{\partial^2 y_c}{\partial z^2} - 2\pi r_{co} k(y_c - y_o) + 2\pi r_{ic} k(y_i - y_c) = 0 \\ E_i A_i \dfrac{\partial^2 y_i}{\partial z^2} - 2\pi r_{ic} k(y_i - y_c) = 0 \end{cases} \quad \text{(B1)}$$

where E_o = Young's modulus of the outer pipe (GPa), A_o = cross-sectional area of the outer pipe (m^2), E_c = Young's modulus of the cement (GPa), A_c = cross-sectional area of the cement (m^2), E_i = Young's modulus of the inner pipe (GPa), A_i = cross-sectional area of the inner pipe (m^2), y_o = axial displacement of the outer pipe (m), y_c = axial displacement of the cement (m), y_i = axial displacement of the inner pipe (m), k = shear stiffness of the cement-steel interface (GPa/m), r_{co} = radius from the longitudinal axis of the model to the cement-outer pipe interface (m), r_{ic} = radius from the longitudinal axis of the model to the inner pipe-cement interface (m). The above simultaneous equations can be arranged in the matrix form as follows:

$$\frac{\partial^2}{\partial z^2}\begin{bmatrix} y_o \\ y_c \\ y_i \end{bmatrix} = 2\pi k \begin{bmatrix} \dfrac{r_{co}}{E_o A_o} & \dfrac{-r_{co}}{E_o A_o} & 0 \\ \dfrac{-r_{co}}{E_c A_c} & \dfrac{r_{co} + r_{ic}}{E_c A_c} & \dfrac{-r_{ic}}{E_c A_c} \\ 0 & \dfrac{-r_{ic}}{E_i A_i} & \dfrac{r_{ic}}{E_i A_i} \end{bmatrix} \begin{bmatrix} y_o \\ y_c \\ y_i \end{bmatrix} \quad \text{(B2)}$$

Equation B2 can be solved via diagonalization of the matrix, which yields the following equations:

$$\frac{\partial^2}{\partial z^2}\begin{bmatrix} Y_o \\ Y_c \\ Y_i \end{bmatrix} = \begin{bmatrix} \lambda_o & 0 & 0 \\ 0 & \lambda_c & 0 \\ 0 & 0 & \lambda_i \end{bmatrix} \begin{bmatrix} Y_o \\ Y_c \\ Y_i \end{bmatrix} \quad \text{(B3)}$$

where $\lambda_o, \lambda_c, \lambda_i$ are the eigenvalues of the matrix and

$$\begin{bmatrix} Y_o \\ Y_c \\ Y_i \end{bmatrix} = \begin{bmatrix} \begin{pmatrix} | \\ p_o \\ | \end{pmatrix} & \begin{pmatrix} | \\ p_c \\ | \end{pmatrix} & \begin{pmatrix} | \\ p_i \\ | \end{pmatrix} \end{bmatrix}^{-1} \begin{bmatrix} y_o \\ y_c \\ y_i \end{bmatrix} = \begin{bmatrix} p_{o1} & p_{c1} & p_{i1} \\ p_{o2} & p_{c2} & p_{i2} \\ p_{o3} & p_{c3} & p_{i3} \end{bmatrix}^{-1} \begin{bmatrix} y_o \\ y_c \\ y_i \end{bmatrix} \quad \text{(B4)}$$

where p_o, p_c, p_i are orthonormal vectors corresponding to the respective eigenvalues. For the

parameter values listed in Table 2, the eigenvalues of the matrix are calculated to be $\lambda_o = 47.41, \lambda_c = 3.862, \lambda_i = 0$. Therefore, the general solutions for Equation B3 are given by the following equations:

$$\begin{bmatrix} Y_o \\ Y_c \\ Y_i \end{bmatrix} = \begin{bmatrix} C_{o1}e^{\sqrt{\lambda_o}z} + C_{o2}e^{-\sqrt{\lambda_o}z} \\ C_{c1}e^{\sqrt{\lambda_c}z} + C_{c2}e^{-\sqrt{\lambda_c}z} \\ C_{i1}z + C_{i2} \end{bmatrix} \tag{B5}$$

By substituting Equation B5 into Equation B4, the general solutions are obtained as follows:

$$\begin{bmatrix} y_o \\ y_c \\ y_i \end{bmatrix} = \begin{bmatrix} p_{o1}\left(C_{o1}e^{\sqrt{\lambda_o}z} + C_{o2}e^{-\sqrt{\lambda_o}z}\right) + p_{c1}\left(C_{c1}e^{\sqrt{\lambda_c}z} + C_{c2}e^{-\sqrt{\lambda_c}z}\right) + p_{i1}(C_{i1}z + C_{i2}) \\ p_{o2}\left(C_{o1}e^{\sqrt{\lambda_o}z} + C_{o2}e^{-\sqrt{\lambda_o}z}\right) + p_{c2}\left(C_{c1}e^{\sqrt{\lambda_c}z} + C_{c2}e^{-\sqrt{\lambda_c}z}\right) + p_{i2}(C_{i1}z + C_{i2}) \\ p_{o3}\left(C_{o1}e^{\sqrt{\lambda_o}z} + C_{o2}e^{-\sqrt{\lambda_o}z}\right) + p_{c3}\left(C_{c1}e^{\sqrt{\lambda_c}z} + C_{c2}e^{-\sqrt{\lambda_c}z}\right) + p_{i3}(C_{i1}z + C_{i2}) \end{bmatrix} \tag{B6}$$

The boundary conditions of the well model under tensile loading are (i) zero axial displacement in the outer and inner pipes at $z = 0$, (ii) zero axial strain in the cement at $z = 0$, L and in the inner pipe at $z = L$ and (iii) constant axial stress in the outer pipe at $z = L$. The zero strain boundary at $z = 0$ in the cement would be valid assuming that the cohesion at the cement-top plate interface ($z = 0$) in the normal direction is negligible compared to the interface cohesion against shearing at the inner and outer pipe-cement interfaces. The aforementioned boundary conditions are expressed as follows:

$$\begin{gathered} y_o|_{z=0} = 0, \;\; y_i|_{z=0} = 0, \;\; \left.\frac{\partial y_c}{\partial z}\right|_{z=0} = 0, \\ \left.\frac{\partial y_o}{\partial z}\right|_{z=L} = \frac{\sigma}{E_o}, \;\; \left.\frac{\partial y_i}{\partial z}\right|_{z=L} = 0, \;\; \left.\frac{\partial y_c}{\partial z}\right|_{z=L} = 0 \end{gathered} \tag{B7}$$

By applying these boundary conditions, the coefficients in Equation B6 are obtained as follows:

$$\begin{bmatrix} C_{o1} \\ C_{o2} \\ C_{c1} \\ C_{c2} \\ C_{i1} \\ C_{i2} \end{bmatrix} = \begin{bmatrix} p_{o1}e^{\sqrt{\lambda_o}L} & p_{o1}e^{-\sqrt{\lambda_o}L} & p_{c1}e^{\sqrt{\lambda_c}L} & p_{c1}e^{-\sqrt{\lambda_c}L} & p_{i1}L & p_{i1} \\ p_{o3}e^{\sqrt{\lambda_o}L} & p_{o3}e^{-\sqrt{\lambda_o}L} & p_{c3}e^{\sqrt{\lambda_c}L} & p_{c3}e^{-\sqrt{\lambda_c}L} & p_{i3}L & p_{i3} \\ p_{o2}\sqrt{\lambda_o}e^{\sqrt{\lambda_o}L} & -p_{o2}\sqrt{\lambda_o}e^{-\sqrt{\lambda_o}L} & p_{c2}\sqrt{\lambda_c}e^{\sqrt{\lambda_c}L} & -p_{c2}\sqrt{\lambda_c}e^{-\sqrt{\lambda_c}L} & p_{i2} & 0 \\ p_{o1}\sqrt{\lambda_o} & -p_{o1}\sqrt{\lambda_o} & p_{c1}\sqrt{\lambda_c} & -p_{c1}\sqrt{\lambda_c} & p_{i1} & 0 \\ p_{o3}\sqrt{\lambda_o} & -p_{o3}\sqrt{\lambda_o} & p_{c3}\sqrt{\lambda_c} & -p_{c3}\sqrt{\lambda_c} & p_{i3} & 0 \\ p_{o2}\sqrt{\lambda_o} & -p_{o2}\sqrt{\lambda_o} & p_{c2}\sqrt{\lambda_c} & -p_{c2}\sqrt{\lambda_c} & p_{i2} & 0 \end{bmatrix}^{-1} \begin{bmatrix} 0 \\ 0 \\ 0 \\ \frac{\sigma}{E_o} \\ 0 \\ 0 \end{bmatrix} \tag{B8}$$

Appendix C: Nomenclature

Roman symbols

A_c	Cross-sectional area of the cement
A_i	Cross-sectional area of the inner pipe
A_o	Cross-sectional area of the outer pipe
C_T	Temperature coefficient
C_ϵ	Strain coefficient
E_c	Young's modulus of the cement
E_i	Young's modulus of the inner pipe
E_o	Young's modulus of the outer pipe
k	Shear stiffness of the cement-steel interface
p_c	Orthonormal vector corresponding to the eigenvalue λ_c
p_e	Effective photo-elastic coefficient
p_i	Orthonormal vector corresponding to the eigenvalue λ_i
p_o	Orthonormal vector corresponding to the eigenvalue λ_o
r_{co}	Radius from the longitudinal axis of the well model to the cement-outer pipe interface
r_{ic}	Radius from the longitudinal axis of the well model to the inner pipe-cement interface
ΔT	Change in temperature
x	Distance along fibre optic cables
y_c	Axial displacement of the cement
y_i	Axial displacement of the inner pipe
y_o	Axial displacement of the outer pipe

Greek symbols

α_L	Linear thermal expansion coefficient
α_n	Thermo-optic coefficient
ϵ_{BOTDR}	Pseudo BOTDR strain profile
ϵ_{real}	Real strain profile
$\Delta\epsilon$	Change in strain
λ_c	Eigenvalue of the matrix shown in Equation B2
λ_i	Eigenvalue of the matrix shown in Equation B2
λ_o	Eigenvalue of the matrix shown in Equation B2
λ_0	Baseline wavelength of the reflected light
$\Delta\lambda'$	Change in wavelength of the reflected light

$\Delta\nu_B$ Brillouin frequency shift

σ_G Standard deviation of the Gaussian distribution

Acknowledgements

The funding for this research has been provided by the MH21 Research Consortium in the Ministry of Economy, Trade and Industry (METI) via Japan Oil, Gas and Metals National Corporation (JOGMEC). The authors would like to express sincere gratitude for the provision of this research funding. The experiment was made possible with substantial technical assistance from staff members in the University of California, Berkeley and Pacific Earthquake Engineering Research Center (PEER). We would like to thank Shakhzod Takhirov (Berkeley), Amarnath Kasalanati (PEER), Nathaniel Knight (PEER), Robert Cerney (PEER), Lobsang Garcia (PEER), Selim Gunay (PEER), Phillip Wong (Berkeley), Llyr Griffith (Berkeley) and Matt Cataleta (Berkeley) for their technical assistance and consultation.

References

Baker Hughes, 2019. *Surface Monitoring Systems*. Available at: https://www.bhge.com/system/files/2018-06/surface-monitoring-panels-slsh.pdf (Accessed: 9 November 2019).

Baldwin, C., 2018. Fiber Optic Sensors in the Oil and Gas Industry: Current and Future Applications, in Alemohammad, H. (ed.) *Opto-Mechanical Fiber Optic Sensors: Research, Technology, and Applications in Mechanical Sensing*. Oxford, UK: Butterworth-Heinemann, pp. 211–236. doi: 10.1016/B978-0-12-803131-5.00008-8.

Baldwin, C. S., 2015 Applications for fiber optic sensing in the upstream oil and gas industry, in *Proceedings of Fiber Optic Sensors and Applications XII*. Baltimore, Maryland, USA, pp. 1–10. doi: 10.1117/12.2176226.

Bourne-Webb, P. J. *et al.,* 2009. Energy pile test at Lambeth College, London: geotechnical and thermodynamic aspects of pile response to heat cycles, *Géotechnique*, 59(3), pp. 237–248. doi: 10.1680/geot.2009.59.3.237.

Chen, L. *et al.,* 2018. Production behavior and numerical analysis for 2017 methane hydrate extraction test of Shenhu, South China Sea, *Journal of Natural Gas Science and Engineering*, 53, pp. 55–66. doi: 10.1016/j.jngse.2018.02.029.

Earles, D. M. *et al.,* 2010. Real-Time Monitoring of Sand Control Completions, in *Proceedings of the SPE Annual Technical Conference and Exhibition*. Florence, Italy, pp. 19–22. Available at: https://doi.org/10.2118/134555-ms.

Farrell, H. *et al.,* 2012. IgnIk SIkumI GaS Hydrate FIeld trIal Completed, *Fire in the Ice*, pp. 1–3. Available at: https://www.netl.doe.gov/sites/default/files/publication/MHNews_2012_June.pdf.

Großwig, S., Hurtig, E. and Kühn, K., 1996. Fibre optic temperature sensing : A new tool for temperature measurements in boreholes, *GEOPHYSICS*, 61(4), pp. 1065–1067. Available at: https://doi.org/10.1190/1.1444027.

Horiguchi, T. *et al.,* 1995. Development of a Distributed Sensing Technique Using Brillouin Scattering, *Journal of Lightwave Technology*, 13(7), pp. 1296–1302. doi: 10.1109/50.400684.

Horiguchi, T., Kurashima, T. and Tateda, M., 1989. Tensile strain dependence of Brillouin frequency shift in silica optical fibers, *Photonics Technology Letters*, 1(5), pp. 107–108. Available at: https://doi.org/10.1109/68.34756.

Horiguchi, T. and Tateda, M., 1989. BOTDA—Nondestructive Measurement of Single-Mode Optical Fiber Attenuation Characteristics Using Brillouin Interaction: Theory, *Journal of Lightwave Technology*, 7(8), pp. 1170–1176. doi: 10.1109/50.32378.

Hotate, K. and Hasegawa, T., 2000. Measurement of Brillouin Gain Spectrum Distribution along an Optical Fiber Using a Correlation-Based Technique—Proposal, Experiment and Simulation—, *Ieice Trans. Electron.*, E83-C(3), pp. 405–412. doi: 10.1.1.29.7344.

Hurtig, E. *et al.,* 1994. Fibre-optic temperature measurements in shallow boreholes: experimental application for fluid logging, *Geothermics*, 23(4), pp. 355–364. doi: 10.1016/0375-6505(94)90030-2.

Hveding, F., Bukhamsin, A. and Aramco, S., 2018. Distributed Fiber Optic Sensing – A Technology Review for Upstream Oil and Gas Applications, in *Proceedings of the SPE Kingdom of Saudi Arabia Annual Technical Symposium and Exhibition*. Dammam, Saudi Arabia, pp. 1–15. Available at: https://doi.org/10.2118/192323-ms.

Hveding, F. and Porturas, F., 2015. Integrated Applications of Fiber-Optic Distributed Acoustic and Temperature Sensing, in *Proceedings of the SPE Latin American and Caribbean Petroleum Engineering Conference*. Quito, Ecuador, pp. 1–16. Available at: https://doi.org/10.2118/177222-ms.

Klar, A. *et al.,* 2006. Distributed strain measurement for pile foundations, *Proceedings of the Institution of Civil Engineers - Geotechnical Engineering*, 159(3), pp. 135–144. doi: 10.1680/geng.2006.159.3.135.

Klar, A. *et al.,* 2019. Marine gas hydrate technology : State of the art and future possibilities for Europe, *Marine gas hydrate – an indigenous resource of natural gas for Europe (MIGRATE)*, p. 54. doi: 10.3289/MIGRATE_WG2.2019.

Li, B. *et al.,* 2017. Dynamic Strain Measurement Using Small Gain Stimulated Brillouin

Scattering in STFT-BOTDR, 17(9), pp. 2718–2724. Available at: https://doi.org/10.1109/jsen.2017.2657119.

Li, J. *et al.,* 2018. The first offshore natural gas hydrate production test in South China Sea, *China Geology*. Elsevier B.V., 1(1), pp. 5–16. doi: 10.31035/cg2018003.

Maraval, D. *et al.,* 2017. Dynamic Optical Fiber Sensing With Brillouin Optical Time Domain Reflectometry: Application to Pipeline Vibration Monitoring, *Journal of Lightwave Technology*, 35(16), pp. 3296–3302. doi: 10.1109/JLT.2016.2614835.

Maslin, M. *et al.,* 2010. Gas hydrates: past and future geohazard?, *Philosophical Transactions of the Royal Society A: Mathematical, Physical and Engineering Sciences*, 368, pp. 2369–2393. doi: 10.1098/rsta.2010.0065.

Mayuga, M. N. and Allen, D. R., 1969. Subsidence in the Wilmington oil field, Long Beach, California, U.S.A., in *Proceedings of the Tokyo Symposium on Land Subsidence, International Association of Scientific Hydrology, Studies and reports in hydrology, IASH-UNESCO*. Tokyo, Japan, pp. 66–79. Available at: http://www.saveballona.org/gasoilfields/WilmSubGC.pdf.

Mohamad, H. *et al.,* 2011. Performance monitoring of a secant-piled wall using distributed fiber optic strain sensing, *Journal of Geotechnical and Geoenvironmental Engineering*, 137(12), pp. 1236–1243. doi: 10.1061/(ASCE)GT.1943-5606.0000543.

Molenaar, M. M. *et al.,* 2012. First Downhole Application of Distributed Acoustic Sensing for Hydraulic-Fracturing Monitoring and Diagnostics, *SPE Drilling & Completio*, 27(1), pp. 32–38. doi: 10.2118/140561-PA.

Motil, A., Bergman, A. and Tur, M., 2016. State of the art of Brillouin fiber-optic distributed sensing, *Optics and Laser Technology*. Elsevier, 78, pp. 81–103. doi: 10.1016/j.optlastec.2015.09.013.

Nagel, N. B., 2001. Compaction and subsidence issues within the petroleum industry: From Wilmington to Ekofisk and beyond, *Physics and Chemistry of the Earth, Part A: Solid Earth and Geodesy*, 26(1–2), pp. 3–14. doi: 10.1016/S1464-1895(01)00015-1.

Omnisens, 2019. *VISION Dual Datasheet*. Available at: http://www.cazor.com.cn/admin/upload/file/2017959283444665.pdf (Accessed: 9 November 2019).

Pearce, J. G. and Rambow, F. H. K., 2009. High Resolution, Real-Time Casing Strain Imaging for Reservoir and Well Integrity Monitoring: Demonstration of Monitoring Capability in a Field Installation, in *Proceedings of the 2009 SPE Annual Technical Conference and Exhibition*. New Orleans, Louisiana, USA, pp. 1–15. Available at: https://doi.org/10.2118/124932-ms.

Pearce, J. and Legrand, P., 2009. Real-time compaction monitoring with fiber-optic distributed

strain sensing (DSS), in *Proceedings of the SPWLA 50th Annual Logging Symposium*. The Woodlands, Texas, USA, pp. 1–11. Available at: https://www.onepetro.org/conference-paper/SPWLA-2009-85310.

Pelecanos, L. *et al.,* 2017. Distributed fibre-optic monitoring of an Osterberg-cell pile test in London, *Géotechnique Letters*, 7(2), pp. 1–9. doi: 10.1680/jgele.16.00081.

Pelecanos, L. *et al.,* 2018. Distributed Fiber Optic Sensing of Axially Loaded Bored Piles, *Journal of Geotechnical and Geoenvironmental Engineering*, 144(3), pp. 1–16. doi: 10.1061/(ASCE)GT.1943-5606.0001843.

Peled, Y., Motil, A. and Tur, M., 2012. Fast Brillouin optical time domain analysis for dynamic sensing, *Optics Express*, 20(8), p. 8584. doi: 10.1364/OE.20.008584.

Roberts, D., 1953. Shear prevention in the Wilmington Field, pp. 146–155. Available at: https://www.onepetro.org/conference-paper/API-53-146.

Sasaki, T. *et al.,* 2019. Simulation of well integrity in offshore unconsolidated methane hydrate-bearing formation during reservoir compaction (in preparation for submission).

Schwall, G. M. and Denney, C. A., 1994. Subsidence Induced Casing Deformation Mechanisms in the Ekofisk field, in *Proceedings of the 1994 Eurock SPE/ISRM Rock Mechanics in Petroleum Engineering Conference*. Delft, The Netherlands, pp. 507–515. doi: 10.2118/28091-MS.

Shangguan, M. *et al.,* 2017. Brillouin optical time domain reflectometry for fast detection of dynamic strain incorporating double-edge technique, *Optics Communications*. Elsevier B.V., 398(January), pp. 95–100. doi: 10.1016/j.optcom.2017.04.033.

Teodoriu, C. *et al.,* 2012. Experimental Measurements of Mechanical Parameters of Class G Cement, in *Proceedings of the SPE/EAGE European Unconventional Resources Conference and Exhibition*. Vienna, Austria, pp. 1–7. Available at: https://doi.org/10.2118/153007-MS.

Thiruvenkatanathan, P. *et al.,* 2016. Downhole Sand Ingress Detection Using Fibre-Optic Distributed Acoustic Sensors, in *Proceedings of the Abu Dhabi International Petroleum Exhibition & Conference*. Abu Dhabi, UAE, pp. 1–9. Available at: https://doi.org/10.2118/183329-ms.

Uchida, S., 2012. *Numerical investigation of geomechanical behaviour of hydrate-bearing sediments*. PhD thesis. University of Cambridge.

Uchida, S., Klar, A. and Yamamoto, K., 2016. Sand production model in gas hydrate-bearing sediments, *International Journal of Rock Mechanics and Mining Sciences*. Elsevier, 86, pp. 303–316. doi: 10.1016/j.ijrmms.2016.04.009.

Uchida, S., Soga, K. and Yamamoto, K., 2012. Critical state soil constitutive model for methane hydrate soil, *Journal of Geophysical Research: Solid Earth*, 117(B3), pp. 1–13. doi:

10.1029/2011JB008661.

Williams, G. R. *et al.,* 2000. Distributed temperature sensing (DTS) to characterize the performance of producing oil wells, in *Proceedings of SPIE Industrial Sensing Systems*. Boston, Massachusetts, USA, pp. 39–54. doi: 10.1117/12.411726.

Yamamoto, K. *et al.,* 2014. Operational overview of the first offshore production test of methane hydrates in the Eastern Nankai Trough, in *Proceedings of the Offshore Technology Conference*. Houston, Texas, USA, pp. 1–11. doi: 10.4043/25243-MS.

Yamamoto, K., 2015. Overview and introduction: Pressure core-sampling and analyses in the 2012-2013 MH21 offshore test of gas production from methane hydrates in the eastern Nankai Trough, *Marine and Petroleum Geology*. Elsevier Ltd, 66, pp. 296–309. doi: 10.1016/j.marpetgeo.2015.02.024.

Yamamoto, K. *et al.,* 2017. Thermal responses of a gas hydrate-bearing sediment to a depressurization operation, *RSC Advances*. Royal Society of Chemistry, 7(10), pp. 5554–5577. doi: 10.1039/C6RA26487E.

Yamamoto, K. and Dallimore, S. R., 2008. Aurora-JOGMEC-NRCan Mallik 2006-2008 gas hydrate research project progress, *Fire in the Ice*, Summer, pp. 1–5. Available at: https://www.netl.doe.gov/research/oil-and-gas/methane-hydrates/fire-in-the-ice.

Yoneda, J. *et al.,* 2014. Evaluation of Frictional Properties for Methane-Hydrate-Well Completion and Production, *SPE Drilling & Completion*, 29(01), pp. 115–124. Available at: https://doi.org/10.2118/169897-pa.

Yoneda, J. *et al.,* 2018. Mechanical Response of Reservoir and Well Completion of the First Offshore Methane-Hydrate Production Test at the Eastern Nankai Trough: A Coupled Thermo-Hydromechanical Analysis, *SPE Journal*, 24(02), pp. 531–546. doi: 10.2118/191145-PA.

Zhang, Y. *et al.,* 2014. Strain variation measurement with short-time Fourier transform-based Brillouin optical time-domain reflectometry sensing system, *Electronics Letters*, 50(22), pp. 1624–1626. doi: 10.1049/el.2014.2470.